Laminin γ1-dependent basement membranes are instrumental to ensure proper olfactory placode shape, position and boundary with the brain, as well as olfactory axon development

Tignard P[1,2], Pottin K[1], Geeverding A[3], Doulazmi M[4], Cabrera M[1], Fouquet C[2], Liffran M[2], Fouchard J[1], Rosello M[5], Albadri S[5], Del Bene F[5], Trembleau A[2,*], Breau MA[1,6,*].

[1]Sorbonne Université, Centre National de la Recherche Scientifique (CNRS UMR7622), Institut de Biologie Paris-Seine (IBPS), Developmental Biology Laboratory, Paris, France

[2]Sorbonne Université, Centre National de la Recherche Scientifique (CNRS UMR8246), Inserm U1130, Institut de Biologie Paris Seine (IBPS), Neuroscience Paris Seine (NPS), Paris, France.

[3]Imaging Facility, Institut de Biologie Paris-Seine (IBPS)

[4]Sorbonne Université, Centre National de la Recherche Scientifique (CNRS UMR8256), Institut de Biologie Paris Seine (IBPS), Adaptation Biologique et Vieillissement, Paris, France.

[5]Sorbonne Université, INSERM, CNRS, Institut de la Vision, 17 Rue Moreau, F-75012 Paris, France

[6]Institut National de la Santé et de la Recherche Médicale (INSERM)

*Co-last authors and co-corresponding authors:

Marie Anne Breau (marie.breau@sorbonne-universite.fr) and

Alain Trembleau (alain.trembleau@sorbonne-universite.fr)

Abstract

Despite recent progress, the complex roles played by the extracellular matrix in development and disease are still far from being fully understood. Here, we took advantage of the zebrafish *sly* mutation which affects Laminin γ1, a major component of basement membranes, to explore its role in the development of the olfactory system. Following a detailed characterisation of Laminin distribution in the developing olfactory circuit, we analysed basement membrane integrity, olfactory placode and brain morphogenesis, and olfactory axon development in *sly* mutants, using a combination of immunochemistry, electron microscopy and quantitative live imaging of cell movements and axon behaviours. Our results point to an original and dual contribution of Laminin γ1-dependent basement membranes in organising the border between the olfactory placode and the adjacent brain: they maintain placode shape and position in the face of major brain morphogenetic movements, they establish a robust physical barrier between the two tissues while at the same time allowing the local entry of the sensory axons into the brain and their navigation towards the olfactory bulb. This work thus identifies key roles of Laminin γ1-dependent basement membranes in neuronal tissue morphogenesis and axon development *in vivo.*

Introduction

The extracellular matrix (ECM) is a network of glycoproteins which provides support to tissues by contributing to mechanical and chemical signals regulating their biology. It regulates multiple processes, including cell migration, survival/proliferation, differentiation and polarity (Walma and Yamada, 2020). In addition to the fundamental role of ECM in development and homeostasis, mutations in matrix genes lead to a variety of genetic disorders, and abnormal ECM remodelling drives disease progression in fibrosis, neurological disorders and cancer (Karamanos et al., 2021; Soleman et al., 2013; Theocharis et al., 2019; Yamada et al., 2022). ECM components are also critical factors in tissue engineering and regenerative medicine (Kaur et al., 2021; Kim et al., 2021), and thus represent valuable targets but also key players in a plethora of therapeutic applications.

The ECM can influence development and disease in many ways, and despite recent advances, the full complexity of ECM functions is far from being understood. This partly comes from the lack of tools to investigate ECM roles *in vivo*. Indeed, loss-of-function of ECM components often leads to embryonic lethal phenotypes, for instance during implantation and gastrulation in mice (see for example Miner and Yurchenco, 2004), precluding the analysis of ECM functions at later stages of development.

Laminins are major components of the basement membrane (BM), a layer of ECM lying on the basal side of epithelia, which is essential for their development and homeostasis. Laminins are crucial to initiate BM assembly (Anderson et al., 2009; Huang et al., 2003; Miner and Yurchenco, 2004; Urbano et al., 2009). They are α/β/γ heterotrimers, with Laminin 111 believed to be the predominant isoform during early development (Miner and Yurchenco, 2004). The zebrafish *sly*^{wi390} (*sleepy/lamc1*) mutation (Wiellette et al., 2004) affects Laminin γ1, present in 10 out of 18 isoforms. *sly* homozygous mutants exhibit defects in notochord, blood vessel and somite morphogenesis (Dolez et al., 2011; Odenthal et al., 1996; Parsons et al., 2002; Pollard et al., 2006; Stemple et al., 1996). Maternal or residual expression of the γ1 chain until around 12 hpf (hours-post-fertilisation) (Dolez et al., 2011; Parsons et al., 2002) likely allows *sly* mutants to develop until 48-72 hpf, thus providing an *in vivo* setting to examine later functions of this ECM component.

In this study, we took advantage of the *sly* mutant to investigate the role of Laminin γ1 in the development of the zebrafish olfactory system, which forms through the growth of the axons from the olfactory placode (OP) to the olfactory bulb in the brain (Miyasaka et al., 2007) in the context of morphogenetic movements shaping the OP and nearby tissues (Aguillon et al., 2020; Breau et al., 2017; Hauptmann and Gerster, 2000; Monnot et al., 2022; Ross et al., 1992). Laminin-rich BMs are known to surround the developing OPs and adjacent brain (Torres-Paz and Whitlock, 2014; Torres-Paz et al., 2021), but their function in the construction of the olfactory system remains uncharacterised.

Laminin stimulates neurite outgrowth for many types of neurons *in vitro* (reviewed in Powell and Kleinman, 1997). *In vivo*, in the developing nervous system, Laminin is important for neuro-epithelial morphogenesis (Bryan et al., 2016; Ivanovitch et al., 2013; Sidhaye and Norden, 2017; Tsuda et al., 2010), neuronal migration (Belvindrah et al., 2007; Chen et al., 2009; Grant and Moens, 2010; Sittaramane et al., 2009) and multiple aspects of axonal development including axon emergence (Moore et al., 2022; Randlett et al., 2011; Wolman et al., 2008), growth, and pathfinding (Bonner and O'Connor, 2001; Chen et al., 2009; García-Alonso et al., 1996; Karlstrom et al., 1996; Paulus and Halloran, 2006).

Here, we provide a detailed characterisation of Laminin expression during the construction of the zebrafish olfactory system, in fixed and live embryos. We then use the *sly* mutant, combined with live imaging to quantify cell/tissue movements and axon behaviours, to investigate Laminin γ1 functions in neuronal tissue morphogenesis and axon development *in vivo*. We found that Laminin γ1-dependent BMs are instrumental to maintain proper OP morphology and position, to define the boundary between the OP and the brain and to allow the growth and pathfinding of the olfactory axons towards the olfactory bulb.

Results

The developing OP and brain tissues are surrounded by Laminin-containing BMs

We first analysed Laminin distribution during early OP morphogenesis. It has been proposed that the zebrafish OP contains a transient population of pioneer neurons in the ventro-medial region of the OP: their axons are the first to grow out of the OP at 22-24 hpf, and ablation experiments suggest that they act as a scaffold for the growth of the axons of the later born OSNs, located in the rosette forming in the dorso-lateral region of the OP (Whitlock and Westerfield, 1998). Madelaine et al. (2011) further showed that the first neurons to differentiate in the OP (the early olfactory neurons or EONs) express the *Tg(neurog1:GFP)* transgene (Blader et al., 2003). However, as discussed in Madelaine et al., 2011, *neurog1:GFP*+ neurons appear much more numerous than the previously described pioneer neurons, and may thus include pioneers but also other neuronal subtypes (Whitlock and Westerfield, 1998; Madelaine et al., 2011).

Between 14 and 22 hpf, in a process referred to as OP coalescence, cell movements transform the elongated OP domains into two rounded placodal structures on each side of the brain (Whitlock and Westerfield, 2000). Using the *Tg(neurog1:GFP)* line, it was shown that OP coalescence occurs through two cell movements: first, cell bodies from the anteroposterior extremities of the OP domain converge towards the OP centre. OP cell bodies then move laterally, away from the brain, while their trailing axons remain attached to the brain and grow through retrograde extension (Aguillon et al., 2020; Breau et al., 2017; Monnot et al., 2022). During OP coalescence, *neurog1:GFP*+ cells present in the adjacent forebrain undergo a directional anterior movement (Breau et al., 2017; Monnot et al., 2022).

To analyse Laminin expression at these coalescence stages, we performed immunostainings with a Laminin polyclonal antibody on *Tg(neurog1:GFP)* embryos. Consistent with previous observations (Torres-Paz and Whitlock, 2014; Torres-Paz et al., 2021), we first noticed the appearance of a fairly continuous (with only tiny interruptions) Laminin-rich BM surrounding the brain from 17-18 hpf, while around the OP, only discrete Laminin spots were detected at this stage (Fig. 1A, A'). By contrast, at the end of coalescence (22 hpf), two distinct BMs were clearly visible, one around the brain and the other one partially enveloping the OP on its basal side (Fig. 1B, B'), suggesting that the Laminin-rich BM of the OP starts to assemble between 18 and 22 hpf, during the late phase of OP coalescence.

131 To further analyse the dynamics of Laminin γ1 expression and BM assembly during OP
132 coalescence, we took advantage of the *TgBAC(lamC1:lamC1-sfGFP)* line, in which Laminin γ1
133 is tagged with superfolder GFP and expressed under the control of its own promoter
134 (Yamaguchi et al., 2022). To co-label OP cells, we used the *Tg(cldnb:Gal4; UAS:RFP)* line
135 (Breau et al., 2013), which expresses RFP in all OP cells and in the periderm from around 16
136 hpf. RFP expression is initially weak and mosaic (Fig. 1E) and becomes progressively stronger
137 and more widespread in the OP (Fig. 1F). Using confocal live imaging (n = 4 imaged embryos, 2
138 independent experiments), we confirmed the progressive BM-like accumulation of LamC1-sfGFP
139 around the OP, with a gradual increase of the BM fluorescence during OP coalescence (Fig. 1E-
140 F' and Movie 1). From 17 hpf, mesenchymal cells exhibiting cytoplasmic Laminin-sfGFP were
141 seen to migrate anteriorly around the OP (Movie 1). According to the literature, these cells could
142 represent neural crest cells (NCC) (Bryan et al., 2020; Harden et al., 2012; Torres-Paz and
143 Whitlock, 2014) and/or mesodermally-derived cells of the periocular mesenchyme (Vöcking et
144 al., 2023). A subset of RFP+ OP cells also displayed cytoplasmic Laminin-sfGFP (Fig. 1E-H' and
145 Movie 1). Altogether, these live imaging experiments suggest that Laminin γ1 around the OP
146 starts to be deposited mostly during late coalescence stages, from at least a subset of OP cells
147 and surrounding mesenchymal cells. Telencephalic cells also exhibited cytoplasmic Laminin-
148 sfGFP expression throughout OP coalescence (Movie 2), suggesting that the forebrain
149 contributes to the deposition of its own Laminin γ1-containing BM at these stages.
150
151 To analyse whether the BMs of the brain and OP tissues are maintained at later stages, we
152 used Laminin immunostaining on *Tg(omp:meYFP*) embryos. The *Tg(omp:meYFP*) line labels
153 ciliated OSNs in the dorso-lateral rosette, but also a subset of ventral, unipolar neurons
154 (Miyasaka et al. 2005, see Figure 1C', D'). We also used confocal live imaging with the LamC1-
155 sfGFP reporter in the *Tg(cldnb:Gal4; UAS:RFP)* background. Using both approaches we
156 observed a strong, continuous BM-like signal enveloping the brain and the OP at these stages,
157 except (i) where the olfactory axons leave the OP and enter the brain (defined respectively as
158 the exit and entry points, see below) and, as we previously reported (Baraban et al., 2023), (ii)
159 above the neuronal rosette assembling in the dorso-lateral OP, where the nostril orifice opens in
160 the skin (Fig. 1C-D', 1F-J). Thus, the OP and adjacent brain tissues are ensheathed by BMs
161 from early stages of olfactory system assembly (as depicted in Fig. 1K), suggesting these BMs
162 could play a role in their morphogenesis or the maintenance of their shape during development.
163
164

165 **Laminin distribution suggests a role in olfactory axon development**
166
167 To investigate the distribution of Laminin in relation with axonal development, we used the
168 *Tg(omp:meYFP*) line to visualise olfactory axons including, as described above, the axons of the
169 ciliated OSNs and of a subset of unipolar, ventral neurons (Sato et al. 2005; Miyasaka et al.,
170 2005; Miyasaka et al., 2007). Previous time-course studies using this line showed that following
171 OP coalescence, the YFP+ axons leave the OP from 22-24 hpf through a restricted region in the
172 ventro-medial OP (the exit point), grow dorsally as a fasciculated bundle until around 32 hpf,
173 then start defasciculating in the presumptive olfactory bulb region in the brain (reviewed in Breau
174 and Trembleau, 2023; Miyasaka et al., 2005; Miyasaka et al., 2007; Sato et al., 2007).
175 Immunostaining for Laminin revealed local disruptions in the BMs ensheathing the OP and the
176 brain, precisely where the YFP+ axons exit the OP (exit point) and enter the brain (entry point)
177 (Fig. 1C-D'). Once into the brain, from around 28 hpf, the most distal extremity of the YFP+ axon
178 bundle (but not the axon shafts) was systematically in close contact with the Laminin-labelled
179 BM of the brain (Fig. 1C-D'), suggesting that the growth cones use it as a substrate to migrate
180 towards the olfactory bulb.
181
182 To better understand when and how the gaps of the exit and entry points form in the BMs, we
183 took advantage of our live imaging experiments performed on *TgBAC(lamC1:lamC1-sfGFP);*
184 *Tg(cldnb:Gal4; UAS:RFP)* embryos (n = 4 embryos, 2 independent experiments). By the end of
185 the coalescence, when the BM starts to assemble around the OP, we noticed that small
186 interruptions of the BM were already present near the RFP+ axon tips, along the ventro-medial
187 wall of the OP (Movie 2). This was confirmed by live imaging on *TgBAC(lamC1:lamC1-sfGFP);*
188 *Tg(cldnb:Gal4; UAS:lyn-TagRFP)* embryos (n = 2 embryos), in which OP neurons/axons are
189 mosaically labelled with membrane TagRFP, allowing the visualisation of individual axons
190 (Movie 3). This suggests that the exit point does not open through local perforation of a pre-
191 existing BM around the OP but through incomplete BM synthesis/assembly in this area. The
192 entry point was slightly more dorsal than the exit point (of about 10-20 µm), and the initial dorsal
193 growth of the RFP+ axons thus occurred between the two BMs (Fig. 1F-H'). This difference in
194 the z position of the exit and entry points was not clearly seen on fixed embryos (Fig. 1C-D'),
195 which we interprete as being a consequence of cell/tissue shape changes due to the fixation
196 process. The opening of the entry point through the brain BM was concomitant with the arrival of
197 the RFP+ axons, suggesting that the axons degrade or displace BM components to enter the
198 brain (Fig. 1G-H' and Movie 2). This was also observed by live imaging on

199 *TgBAC(lamC1:lamC1-sfGFP); Tg(cldnb:Gal4; UAS:lyn-TagRFP)* embryos (n = 2 embryos)
200 showing a sparse labelling of OP neurons/axons (Movie 3). Note that, as for the exit points, the
201 entry points often appeared as regions with several, small BM interruptions, rather than as a
202 unique hole in the BM (Movie 4). Once in the brain, as observed in fixed embryos, the distal tip
203 of the RFP+ axons (but not the axon shaft) migrated in close proximity with the brain's BM (Fig.
204 1H, I, Movies 2 and 4). Overall our observations indicate that the axons first grow dorsally for a
205 short distance between the BMs of the OP and the brain, then their distal tips migrate along the
206 internal side of the brain's BM (Fig. 1K). We thus hypothesise that the Laminin-rich BMs serve
207 as a migratory path for the axons during their journey from the OP to the olfactory bulb.
208
209 **The integrity of BMs around the brain and the OP is affected in the *sly* mutant**
210
211 We used the *sly* mutant to analyse the function of Laminin γ1 in the development of the
212 zebrafish olfactory system. As previously observed (Dolez et al., 2011; Parsons et al., 2002;
213 Stemple et al., 1996; Wiellette et al., 2004), Laminin BM-like accumulation could not be detected
214 in *sly* $^{-/-}$ mutants (referred to as *sly* mutants) at all the analysed stages, from 16 to 36 hpf, while
215 heterozygous *sly* $^{+/-}$ embryos displayed an expression pattern that was similar to *sly* $^{+/+}$ embryos
216 (Fig. 2A-C'). This indicates that that there is likely no residual/maternal Laminin at the onset of
217 OP coalescence. Since Laminins are essential for BM assembly in other contexts (Lee and
218 Gross, 2007; Li et al., 2005; Miner and Yurchenco, 2004; Smyth et al., 1999; Urbano et al.,
219 2009), we further checked the presence and structure of the BMs in *sly* mutants. We carried out
220 immunostaining for two other BM components, Collagen IV and Nidogen, at 22, 28 and 36 hpf.
221 Nidogen was present in BM-like structures around the OP and the brain in control siblings, with a
222 pattern resembling that of Laminin, while in *sly* mutants no BM staining could be detected
223 around the two tissues (Fig. 2D-F'). In controls, Collagen IV was present in the linear BMs
224 around the OP and the brain, and, with a more fibrous distribution, in the mesenchymal tissues
225 surrounding the OP. In *sly* mutants, Collagen IV immunoreactive pattern was dramatically
226 disrupted, but not totally abolished: the BM-like linear staining was absent, but discrete patches
227 of fibrous expression remained around the OP, at various locations (Fig. 2G-I').
228
229 We next used electron microscopy (EM) to analyse the ultrastructure of BMs in *sly* mutants and
230 control siblings. We focused on the interface between the forebrain and the OP, where NCC are
231 known to migrate during OP coalescence (Bryan et al., 2020; Harden et al., 2012; Torres-Paz
232 and Whitlock, 2014). NCC, OP and brain cells could be identified on the large field EM images

233 by their position and morphology (Fig. 2L, L'). At 24 hpf in controls, the plasma membranes of
234 NCC were separated from those of adjacent OP and brain cells by a 120 nm-wide gap
235 containing electron dense ECM material (Fig. 2J, M). This material likely represents the BMs of
236 the two tissues, with morphological features resembling those of BMs found in other tissues of
237 zebrafish embryos at similar stages (Bryan et al., 2020; Yamaguchi et al., 2022). In *sly* mutants,
238 almost no NCC could be detected, suggesting that NCC development is affected. In this mutant
239 context, the plasma membranes of OP and brain cells were separated by a 40 nm-wide gap,
240 which was significantly smaller than in controls. This gap was most often devoid of electron
241 dense material (only rare spots could be detected, Fig. 2J, J', M). A similar trend was detected at
242 32 hpf (Fig 2K, K', N). By contrast, the thickness of the intercellular gaps within the OP or the
243 brain was not affected in mutants (Fig. S1). The integrity of the OP and brain BMs is thus
244 strongly affected in *sly* mutants, as previously reported in other tissues of Laminin γ1 mutants
245 (Urbano et al., 2009; Yamagushi et al., 2022). We next analysed the consequences on the
246 development of the olfactory system components (placode, brain, olfactory axons).
247
248 **OP coalescence still occurs in the *sly* mutant**
249
250 To study the role of Laminin γ1-dependent BMs in OP coalescence, we first measured the
251 dimensions of the *Tg(neurog1:GFP)*+ OP cell clusters at 22 hpf (end of coalescence) on fixed
252 *sly* mutants and control siblings. While no difference was found for anteroposterior (AP) and
253 dorsoventral (DV) dimensions, the mediolateral (ML) dimension was increased in mutants (Fig.
254 3A-E). This could be the consequence of an increased number of GFP+ cells, however no
255 difference was found in the number of mitotic cells in the OPs of *sly* mutants and control siblings
256 at 16 and 21 hpf (Fig. S2A, B, E, F) and, as previously reported in other tissues (Parsons et al.,
257 2002), we observed a tendency for the *sly* mutants to exhibit increased apoptosis (Fig. S2I, J, M,
258 N). The higher ML dimension could also be due to increased lateral movements of OP cell
259 bodies in the absence of the BM surrounding the OP. To test this, we performed live imaging on
260 *sly* mutants and control siblings carrying the *Tg(neurog1:GFP)* transgene, mounted in a dorsal
261 view (n = 5 mutants and n = 5 controls) (Fig. 3F-I and Movie 5). Individual nuclei of GFP+ OP
262 and brain cells were tracked using widespread expression of H2B-RFP, obtained through mRNA
263 injection. From the cell trajectories we extracted the 3D Mean Square Displacements (MSD), a
264 measure of the volume explored by a cell in a given period of time. No significant difference was
265 observed for the MSD of OP cells between controls and *sly* mutants, but the MSD was higher for
266 brain cells in the mutants (Fig. 3J, K). Direction wise, surprisingly OP cells did not show any

267 change in their total ML displacement (Fig. 3L), nor in their DV displacement (Fig. 3M).
268 Differences, although not statistically significant, could be detected along the AP axis for
269 anterior, central and posterior OP cells: in the mutants the anterior cohort of cells tended to
270 migrate less posteriorly, while central and posterior cells migrated more anteriorly, as if the final
271 cell positions were all shifted towards more anterior locations (Fig. 3N-P). In conclusion, while
272 the movements of brain cells are increased in the absence of BMs at coalescence stages,
273 overall the OP cell movements occur with normal parameters and allow the condensation of
274 OPs into compact neuronal clusters in the *sly* mutants. It is possible however that the position of
275 the OP along the AP axis is shifted anteriorly at the end of OP coalescence.
276
277 **Role of Laminin γ1-dependent BMs during the forebrain flexure**
278
279 Following OP coalescence, the forebrain flexure, a major morphogenetic process which is
280 essential for the final folded shape of the vertebrate brain, starts to remodel the head tissues
281 (Chapman et al., 2005; Garcia et al., 2017; Hauptmann and Gerster, 2000; Tropepe and Sive,
282 2003). In zebrafish the bending of the forebrain has been reported to occur between 24 and 48
283 hpf through the observation of fixed samples (Ross et al., 1992; Hauptmann and Gerster, 2000).
284 We set out to investigate the role of the brain and OP BMs during the forebrain flexure. The
285 *Tg(omp:meYFP*) transgene expression was used to quantify the dimensions of the YFP+ cluster
286 in the OP at various stages of the flexure (24, 28, 32 and 36 hpf). While no change could be
287 detected in the AP and ML dimensions of the YFP+ cluster (except for the ML dimension at 28
288 hpf), its DV dimension was significantly increased in *sly* mutants at all the analysed stages (Fig.
289 4A-E and Fig. S3A-L). This higher DV dimension is unlikely to result from an increase in the
290 number of cells, since YFP+ mitotic cells were not more numerous in *sly* mutants (Fig. S2C, D,
291 G, H), and YFP+ OP clusters displayed increased apoptosis, as observed at earlier stages (Fig.
292 S2K, L, O, P). Counting the YFP+ cells on high magnification images of 3 mutant and 3 control
293 OPs at 28 and 36 hpf further confirmed that the YFP+ cell number is unchanged (Fig. S2Q, R).
294 In addition to the DV elongation of the OP tissue, isolated, ectopic (mispositioned) YFP+ cells
295 were observed all around the YFP+ cluster in the *sly* mutants (Fig. 4F-H and Movie 8). The
296 rosette structure appeared to form normally on the dorso-lateral region of the OP in *sly* mutants
297 (Movie 8).
298
299 To better understand the origin of these phenotypes, we analysed the dynamic behaviours of
300 brain and OP cells occurring during the forebrain flexure, which had not been characterised so

301 far. We carried out live imaging from 22 to 40 hpf on *Tg(omp:meYFP)* *sly* mutants and control
302 siblings injected with H2B-RFP mRNA to label all nuclei, and tracked YFP+ OP cells and
303 adjacent brain cells (n = 4 mutants and n = 4 controls) (Fig. 4I-L and Movie 6). From 24-26 hpf
304 we observed a marked anterior and ventral departure of brain cells in control embryos,
305 representing the onset of the flexure movement. Strikingly, OP cells also moved anteriorly and
306 ventrally from these stages, in coordination with the brain, revealing that the OPs are also
307 subjected to the flexure movement (Fig. 4J and Fig. S3M, Movie 6). The flexure movements
308 were also visible in the brain and OPs of *sly* mutants (Fig. 4L and Fig. S3N, Movie 6), with OP
309 cells moving with a higher MSD than in controls (Fig. 4M). A similar trend was observed for brain
310 cells, but was not statistically significant (Fig. 4N). Moreover, upon visualisation of the cell
311 trajectories in a lateral (YZ) view, we noticed that in 4/4 mutant embryos, brain and OP cells
312 exhibited curved trajectories, moving first anteriorly and ventrally, then turning posteriorly, while
313 this phenomenon occurred in only 1/4 control sibling during the duration of our movies (Fig.
314 S3M, N). This reinforces the idea that brain and OP cells are subjected to an accelerated or
315 enhanced forebrain flexure remodelling in the *sly* mutants, and suggests that in the wild type
316 situation the BMs allow the tissues, and in particular the OP, to resist to the morphogenetic
317 movements associated with the flexure. Altogether, our findings show that the Laminin γ1-
318 containing BMs are required to prevent OP cell scattering, maintain OP shape and dampen OP
319 cell movements during the forebrain flexure.
320
321 **Laminin γ1-dependent BMs are required to define a robust boundary between the OP and**
322 **the brain**
323
324 OP cells undergo anterior and ventral movements during the forebrain flexure. We noticed that,
325 while in control siblings OP cells also display a lateral displacement, they rather move in the
326 medial direction in *sly* mutants, towards the brain, as if the two OPs were progressively
327 converging towards each other (Fig. 4J, L, O). This prompted us to image OP and brain tissues
328 in 3D to visualise the boundary between the two tissues and analyse the width of the brain. To
329 do so, we first performed immunostainings at 28 and 36 hpf for the pan-neuronal marker HuC to
330 visualise neurons in the OP and brain on *Tg(cldnb:Gal4; UAS:RFP)* embryos, in which RFP is
331 expressed in the OP. Qualitative observations of these z-stacks revealed that OPs in *sly* mutants
332 are partially embedded within the brain tissue and display a curved and irregular boundary with
333 the brain, while the frontier between the two tissues appears as a straight line in control siblings
334 (Fig. 5A, A', Fig. S4A, A' and Movie 7). To quantify the width of the brain, we used the

335 *Tg(eltC:GFP)* line (Stedman et al., 2009), which expresses GFP in forebrain cells, and crossed it
336 with the *Tg(cldnb:Gal4; UAS:RFP)* line to label the OPs (Fig. 5B, B' and Fig. S4B, B'). We
337 measured the width of the forebrain in 3 distinct AP levels and 3 distinct DV levels in between
338 the two OPs (as depicted in Fig. 5B, B' and Fig. S4B, B' for the DV levels). The width of the
339 forebrain in *sly* mutants was smaller than in controls, in particular in anterior and dorsal areas
340 (Fig 5B-D and Fig. S4B-D). Proliferation was unchanged in the brain of *sly* mutants, while
341 apoptosis was only sligtly increased (Fig. S4E-L), suggesting that the smaller brain width is due
342 to a local distortion of the tissue rather than a decreased number of cells. Next, we quantitatively
343 analysed the straightness of the brain/OP boundary. Note that the *Tg(eltC:GFP)* line could not
344 be used for that purpose because a few cells in the OP also express the transgene. In addition,
345 *Tg(cldnb:Gal4; UAS:RFP)* expression is mosaic in the OP, preventing the use of this line to
346 assess the shape of the brain/OP boundary. To perform such a quantification we thus turned to
347 immunostainings for Dlx3b, a transcription factor specifically expressed in OP (and skin) cells
348 (Torres-Paz and Whitlock, 2014). We used deep learning to segment the 3D z-stacks of Dlx3b-
349 immunostaining in control and *sly* mutant embryos at 36 hpf (Fig. 5E-F'), and quantified the
350 distortion of the OP/brain frontier at various z levels. This analysis demonstrated that the
351 OP/brain boundary is less straight in *sly* mutants as compared with controls (Fig. 5G, H). Thus,
352 our analyses of cell tracks, brain size and proliferation/apoptosis, and of the shape of the
353 brain/OP boundary suggest that the forebrain is smaller and distorted in *sly* mutants, possibly
354 due to the inward convergence of the two OPs. An non-mutually alternative hypothesis is that
355 the brain fails to form in the normal size and shape in *sly* mutants. These findings suggest that
356 the Laminin γ1-dependent BMs serve to establish a straight brain/OP boundary preventing local
357 intermixing and the late convergence of the two OPs towards each other during the flexure
358 movement.
359
360 **Role of Laminin γ1-dependent BMs in olfactory axon development**
361
362 The growth of the olfactory axons starts with the retrograde axon extension of their proximal
363 portions during OP coalescence, from 14 to 22 hpf (Breau et al., 2017), followed by the dorsal
364 growth from the brain/OP boundary to the olfactory bulb from 22 to 32 hpf (Fig. 1K). Laminin has
365 been reported to orient the emergence of axons (Randlett et al., 2011; Moore et al., 2022). Do
366 the Laminin γ1-dependent BMs play any role in axon emergence or anchoring during retrograde
367 axon extension? To test this, we performed live imaging experiments during OP coalescence on
368 *Tg(cldnb:Gal4; UAS:RFP)* embryos injected with the *neurog1:GFP* plasmid (Blader et al., 2003),

369 allowing a sparse labelling of *neurog1:GFP*+ axons (n = 4 mutants and n = 4 controls, 2
370 independent experiments). Several instances of retrograde extension were seen both in controls
371 and mutants (Fig. S5A, B), indicating that retrograde axon extension occurs normally for at least
372 some of the *neurog1:GFP*+ neurons/axons in *sly* mutants. In addition, on fixed *Tg(omp:meYFP*)
373 *sly* mutants at 24 hpf, numerous YFP+ neurons had their proximal axonal portion formed and
374 attached to the brain surface (Fig. S5C-F), suggesting that retrograde axon extension also
375 occurs normally for at least some of the YFP+ OP neurons. Although we can not rule out that
376 retrograde axon extension is affected in a subset of OP neurons, for instance in ectopic cells,
377 the presence of a BM around the OP and/or the brain appears not to be an absolute requirement
378 for the attachment of axon tips to the ventro-medial wall of the OP during retrograde extension.
379
380 Are Laminin γ1-dependent BMs important for the growth or navigation of the axons from the
381 brain/OP boundary to the olfactory bulb, as suggested by Laminin expression? We first
382 examined the axons in *Tg(omp:meYFP*) embryos at 24, 28, 32 and 36 hpf. In mutant embryos,
383 severe axonal defects were observed. Most YFP+ axonal protrusions were unable to leave the
384 OP and appeared to stall at the OP/brain boundary, leading in some embryos to an apparent
385 absence of axon bundle (Fig. S5G, left column and Movie 8). In some embryos (8-10%), a small
386 proportion of axons managed form a bundle reaching the presumptive OB region by ectopically
387 exiting the OP dorsally (an exit point location never observed in the control fish), while the axons
388 would normally exit the OP at a more ventro-medial position in the controls (Fig. S5G, left
389 column and Movie 8). In addition, an increased proportion of embryos with ectopic medial
390 projections was observed in mutants (18 to 30% of the embryos depending on the stage, as
391 compared to 0 to 9% in controls, Fig. S5G, right column). Finally, there is a tendency for a higher
392 percentage of embryos displaying ventral projections in the *sly* mutant, particularly visible at 24
393 hpf (Fig. S5G, middle column). Altogether, these results suggest navigation issues.
394 So far the growth of the zebrafish olfactory axons from the OP to the bulb has been mostly
395 characterised using fixed samples or live imaging with long time intervals (Dynes and Ngai,
396 1998; Miyasaka et al., 2007). To analyse the dynamic behaviour of the axons, we performed live
397 imaging from 22 hpf on *sly* mutant and control embryos injected with the *omp:meYFP* plasmid,
398 in order to obtain a mosaic labelling of the YFP+ neurons and their axons (n = 5 mutants and n =
399 5 controls, Fig. 6A, B). We tracked individual YFP+ growth cones, as well as the YFP+ cell
400 bodies in the OP, during consecutive periods of 200 min each, with a time interval of 10 min. We
401 substracted the average movement of OP cell bodies from the growth cone tracks, in order to
402 remove the contribution of the global flexure remodelling and analyse specifically the behaviours

403 of the axons with respect to the surrounding cells/tissue. In controls, as expected, growth cones
404 overall showed a dorsal and medial migration, except at the end of the movie, which likely
405 corresponds to their arrival and stalling in the presumptive olfactory bulb. By contrast, growth
406 cones in the *sly* mutants did not display a directional migration towards the bulb, during the
407 whole movie duration (Fig. 6C, F, I, L). They were motile and explored the environment, as
408 shown by speed and persistence measurements, but moved on short distances and/or without
409 preferential direction, resulting in a perturbed axon growth (Fig. 6C-N). These live imaging
410 analyses confirm that the migration of the olfactory axons is impaired in *sly* mutants. Altogether,
411 our results show that Laminin γ1-dependent BMs are essential for the growth and navigation of
412 the axons from the OP to the olfactory bulb.
413
414 ***Sly* mutants display cranial NCC defects but this does not contribute to the late olfactory**
415 **system phenotypes**
416
417 Cranial NCC migration is concomitant with OP coalescence. From 14 hpf, NCC progressively
418 populate the gaps between the OP and the eye and brain tissues (Harden et al., 2012; Torres-
419 Paz and Whitlock, 2014; Bryan et al., 2020). Our electron microscopy observations suggested
420 that NCC are absent at the brain/OP interface of *sly* mutants. *In situ* hybridisation for the NCC
421 marker *crestin* (Luo et al., 2001) revealed that, while a clear NCC cluster can be seen at the
422 brain/OP interface in controls at 32 hpf, *crestin*-labelled NCC are absent from this area in *sly*
423 mutants (Fig. S6A, A'). This suggests that Laminin γ1-dependent BMs are important for NCC
424 migration or survival in this region of the embryo.
425
426 To analyse the dynamics of NCC migration in *sly* mutants and control siblings, we performed live
427 imaging from 16 to 32 hpf on embryos carrying the *Tg(neurog1:GFP)* and *Tg(UAS:RFP)*
428 transgenes and injected with a *sox10(7.2):KalTA4* plasmid (Almeida et al., 2015), which allows
429 the mosaic labelling of NCC (n = 10 control placodes and n = 8 mutant placodes, 3 independent
430 experiments) (Movie 9). As expected from previous studies (Harden et al., 2012 ; Torres-Paz
431 and Whitlock, 2014, Bryan et al., 2020), in 10/10 control placodes many labelled NCC had
432 already reached the vicinity of the OP at 16 hpf, and further invaded the interface between the
433 eye and the OP during the movies (Fig. S6B). Surprisingly, in *sly* mutants, numerous motile NCC
434 were also observed close to the OP at 16 hpf in all the analysed placodes (8/8), and populated
435 the eye/OP interface in 7/8 placodes (10/10 in controls) (Fig. S6B). In a subset of control
436 placodes we could detect a few NCC populating the forebrain/OP interface, either ventrally (4/10

437 placodes) or dorsally (8/10 placodes). By contrast, in *sly* mutants, NCC were observed in the
438 dorsal region of the brain/OP boundary in only 2/8 placodes, and in the ventral brain/OP frontier
439 in only 2/8 placodes as well. Interestingly, in these two samples, NCC that had initially populated
440 the ventral brain/OP interface were then expelled from the boundary at later stages (Movie 9 and
441 Fig. S6B). Altogether, these live imaging data suggest that the migration of cranial NCC towards
442 the OP and between the eye and OP is only partially impaired in *sly* mutants. The subset of
443 NCC that populate the OP/forebrain appears to be more specifically affected, with defects in
444 their migration to the interface and/or the maintenance of their position at the interface. Note that
445 since the *crestin* marker labels mostly NCC at the OP/forebrain interface at 32 hpf (Fig. S6A),
446 this could explain why *crestin* expression is almost lost in *sly* mutants at this stage.
447
448 To test whether the phenotypes observed in *sly* mutants are linked to NCC defects, we took
449 advantage of the *foxd3* mutant, in which cranial NCC migration is delayed (Bryan et al., 2020;
450 Monnot et al. 2022), leading to a loss of *crestin*-labelled NCC at 32 hpf which resembles that of
451 the *sly* mutants (Fig. S7A, B). Importantly, Laminin expression appeared to be unchanged in
452 *foxd3* mutants (Fig. S7C', D' and Monnot et al., 2022). We previously showed that this mutant
453 displays a slightly higher (of about 8-10 µm) ML dimension of the OP at the end of coalescence
454 (Monnot et al., 2022) which is similar to what we observed in *sly* mutants (Fig. 3D). This
455 suggests that NCC defects could be the cause of the increased ML dimension in *sly* mutants.
456 We hypothesize that with less NCC around the OP at this stage, the OP tissue is less
457 constrained and thus slightly spread along the ML axis. To further investigate the influence of
458 NCC on the development of the olfactory system at later stages, we analysed OP dimensions
459 and the length of the olfactory axon bundle at 28 and 36 hpf, in *foxd3* $^{-/-}$ mutants and *foxd3* $^{+/-}$ or
460 $^{+/+}$ control siblings expressing the *Tg(omp:meYFP*) transgene. No significant difference was
461 observed between controls and *foxd3* $^{-/-}$ mutants for these parameters (Fig. S7C-L), suggesting
462 that the late OP morphogenesis and axonal phenotypes of the *sly* mutants are not a
463 consequence of the impairment of NCC development.
464
465
466
467

468 **Discussion**

469

470 Our study highlights key roles of Laminin γ1-dependent BMs in critical aspects of the
471 development of the zebrafish olfactory system, revealed here through the detailed analysis of
472 the Laminin γ1 loss-of-function mutant *sly*. During the late development of the OP, Laminin γ1-
473 dependent BMs turned out to be essential to maintain its shape and proper position, and to
474 establish a robust brain/placode boundary. In addition, Laminin-dependent BMs also appeared
475 to be instrumental to ensure a proper growth and pathfinding of the olfactory axons towards the
476 developing olfactory bulb. In the following paragraphs, we will discuss these new roles assigned
477 to BMs in the context of the development of the zebrafish olfactory system, in light of the
478 literature.

479

480 **The BM of the OP acts as a "shell" maintaining its shape and proper position in the face**
481 **of forebrain flexure movements**

482

483 Our data document a mild perturbation of cell movements during OP coalescence, which
484 suggests that Laminin γ1-dependent BMs are overall dispensable for the OP to acquire its initial
485 shape. However, our observation that the OP of the *sly* mutant becomes significantly elongated
486 in the DV dimension and is surrounded by ectopic cells during the forebrain flexure provides
487 strong evidence for a role of the BMs in preventing OP deformation and scattering during this
488 major remodelling of the head tissues. We discovered, along our live imaging observations, a
489 joint anterior and ventral movement of the OPs and forebrain during the flexure time period in
490 the control animals, as if the OPs were dragged along in the same antero-ventral movement as
491 the forebrain. We thus propose that the BM of the OP prevents its deformation in response to
492 the mechanical forces generated by the morphogenetic movement of the neighboring brain.

493

494 The ability of the placode's BM to limit the deformation of the OP during this developmental step
495 most probably relies on its stiffness. In the *Drosophila* egg chamber, while Laminin itself has a
496 minor contribution to the BM mechanical properties, Collagen IV, which deposition in the BM
497 depends on Laminin (Díaz de la Loza et al., 2017) has a major contribution to these properties,
498 and in particular to its stiffness (Töpfer et al., 2022). Actually, this BM is characterized by a
499 gradient of stiffness, due to a gradient of Collagen IV, endowing the BM with anisotropic
500 resistance to tissue expansion, allowing egg chamber elongation (Crest et al., 2017). Even
501 though the putative loss of mechanical properties leading to OP deformation observed in the *sly*

502 mutant is a consequence of a Laminin loss-of-function, it remains conceivable that it is the
503 Collagen IV, rather than the Laminin itself, which is responsible of these mechanical properties
504 in wild-type animals. This hypothesis, in line with the dramatic disorganization of the Collagen IV
505 pattern observed by immunofluorescence in the *sly* mutant, however requires to be challenged
506 by further investigation.
507
508 BMs were for long considered as inert and passive biological material, unable to generate forces
509 by themselves. We now know that their composition is dynamic during morphogenesis (Díaz de
510 la Loza et al., 2017; Harunaga et al., 2014; Khalilgharibi and Mao, 2021; Van De Bor et al.,
511 2021) and this dynamics has been proposed to generate autonomous stresses, i.e. within the
512 BM itself (Loganathan et al., 2016; Pastor-Pareja and Xu, 2011; Zamir et al., 2008). Accordingly,
513 Serna-Morales et al. (Serna-Morales et al., 2023) recently showed that the *Drosophila* ventral
514 nerve cord morphogenesis is driven by a sudden increase in ECM-driven surface tension due to
515 exponential assembly of Collagen IV in the BM. Still in *Drosophila*, it was recently shown that the
516 elastic ECM enveloping the wing imaginal disc is a form of "active" shell whose anisotropic
517 growth affects the tissue layers upon morphogenesis (Harmansa et al., 2023). Whether such
518 mechanisms participate to the control of the OP shape during the brain flexure remains to be
519 addressed, through the analysis of the dynamics of expression of Collagen IV or other
520 components of the BM as well as biomechanical investigations.
521
522 A dramatic consequence of the absence of proper OP and brain BMs in the *sly* mutant is the
523 irregular and undefined frontier between the brain and OP, with placodal cells tending to locally
524 intermingle with brain cells, and vice versa, along the OP/brain interface. This highlights a key
525 role of these BMs in establishing a robust and straight boundary between the OP and the brain.
526 Tissue intermixing has also been observed in the pharynx of Laminin mutants in C. elegans
527 (Huang et al., 2003) and in the Xenopus notochord upon loss-of-function of the Dystroglycan, a
528 major Laminin receptor (Buisson et al., 2014). The absence of a clear boundary between the OP
529 and the brain in the *sly* mutant is accompanied by an apparent distortion of the brain, with
530 notable reduced dimension in its medio-lateral axis. This phenotype, possibly due to the inward
531 migration of the placodes that become partially embedded in the brain, illustrates an additional
532 and unexpected role of the OP and brain BMs, in preventing late convergence of the two
533 placodes towards each other during the flexure movement.
534

535 **BMs act as cues participating to the pathfinding of olfactory axons along their journey**
536 **from the OP to the olfactory bulb**
537
538 The early development of zebrafish olfactory axons begins with their retrograde extension,
539 involving the attachment of the tips of the axonal protrusions to the brain's surface, followed by a
540 lateral movement of the OP cell bodies in the opposite direction (Breau et al., 2017). This initial
541 step appears not to be affected in the *sly* mutant. These results suggest that Laminin-dependent
542 BMs are dispensable for this retrograde axon extension and, more specifically, that Laminin γ1
543 itself or other components of the BMs are unlikely to play a role in the anchoring of those axon
544 tips onto the brain's surface, which is a prerequisite for their retrograde extension.
545
546 Our study shows that following retrograde elongation in the OP, the axons grow and navigate
547 using bona fide growth cones, assemble a tight axon fascicle which crosses the BM of the OP,
548 turns and migrates dorsally for a short distance between both BMs and thereafter crosses the
549 brain BM to navigate towards the olfactory bulb. In other words, the olfactory axons have to
550 cross two BMs. Our data show that the axons cross the first BM as it is still under construction
551 and contain perforations, thus taking advantage of BM-free small pores to exit the OP and reach
552 the narrow area located between the two BMs. By contrast, the entry point into the brain, across
553 the second BM, opens with the arrival of the axons, suggesting that this opening is achieved by
554 the axons themselves. It will be interesting, in future work, to determine whether the axons
555 locally degrade the BM through the secretion of matrix metalloproteases, or displace the BM
556 with protrusive forces, or use a combination of both mechanisms (Chang and Chaudhuri, 2019;
557 Ihara et al., 2011; Nazari et al., 2022; Yamada et al., 2022).
558
559 As they migrate in the narrow corridor between the OP and brain BMs, olfactory axons remain
560 confined in close proximity to the Laminin-rich BMs. Entering into the brain tissue, olfactory
561 axons migrate collectively within a dynamic bundle growing towards the presumptive olfactory
562 bulb. Importantly, once they have reached the brain tissue, the distalmost tip of this axon bundle
563 still grows in close apposition to the internal surface of the brain's BM, suggesting that this BM
564 serves as a migratory path promoting the growth of these axons. This hypothesis is reinforced
565 by the fact that axon growth and directionality are dramatically impaired in the *sly* mutant, in
566 which only few axons expressing *Tg(omp:meYFP*) can extend properly towards their target area.
567 This phenotype is unlikely to be the result of defects in neuronal differentiation, as demonstrated
568 by HuC immunolabeling and expression of the *Tg(neurog1:GFP)* and *Tg(omp:meYFP*)

569 transgenes, which do not show obvious difference as compared to control animals, but appears
570 to be rather due to axon growth and navigation defects. We did not formally identify the
571 component(s) of the BM involved in this axon extension and pathfinding, but we consider
572 Laminin itself as a good candidate for acting as a privileged substrate the axons, as Laminin
573 does so for other populations of axons in zebrafish (Paulus and Halloran, 2006; Semina et al.,
574 2006), and has been shown in rodents to favor OSN axon extension *in vitro*, and to be present *in*
575 *vivo* along the path followed by OSN axons from the olfactory epithelium to the bulb (Kafitz and
576 Greer, 1997). From a molecular point of view, it has been established on cultured sympathetic
577 neurons that Laminin accelerates the growth of axons through binding to integrins, which favors
578 the formation of F-actin in the growth cone in a microtubule- and Rac1-dependent manner
579 (Grabham et al., 2003). Recently, Abe et al. (2021) further documented another role of Laminin
580 in promoting hippocampal neuron growth cones enhanced progression on stiff substrate,
581 through its interaction with L1, highlighting a new mechanosensitive axon outgrowth mediated by
582 a L1-Laminin clutch mechanism (Abe et al., 2021). Whereas such Laminin-dependent
583 mechanisms are used for guiding olfactory axons in zebrafish remains to be further explored.
584 Other components of the BM, also affected in the *sly* mutant, may be involved as well in the
585 regulation of olfactory axon development. Still in rodents indeed, the characterisation of the
586 expression of ECM proteins along the developing olfactory pathway unraveled a complex
587 interplay between ECM permissive and inhibitory cues expressed in a dynamic way, appearing
588 to restrict axons to the pathway while promoting axon outgrowth within (Shay et al., 2008).
589
590 In addition to ECM molecules present in the BMs, guidance cues interacting with these
591 molecules may also be involved in some aspects of the axonal defects observed in the *sly*
592 mutant. For example, while Xenopus retinal axons are repulsed by ephrin-A5 on fibronectin, they
593 are attracted by ephrin-A5 on Laminin (Weinl et al., 2003), and Laminin converts netrin-mediated
594 attraction of these axons to repulsion (Höpker et al., 1999). Moreover, whereas slit2 repulses
595 Robo expressing axons of dorsal root ganglia neurons, this repulsive effect is lost in absence of
596 Laminin (Nguyen-Ba-Charvet et al., 2001). Netrin1a and 1b are expressed in the zebrafish
597 forebrain close to the route of the axons, where they play an attractive role for olfactory axons
598 which express the netrin receptor DCC (Dang et al., 2023; Lakhina et al., 2012). In addition,
599 several ephrin and slits ligands are expressed in the forebrain at stages of axonal growth
600 (zfin.org, Miyasaka et al., 2005). We may thus envisage that the absence of Laminin in the *sly*
601 mutant may change in some way the netrin-, ephrin- or slit-dependent pathfinding of olfactory
602 axons.

603

604 In conclusion, our findings indicate that the boundary between the sensory and central
605 components of the olfactory system (Suter and Jaworski, 2019) is organised by the BMs of the
606 OP and the brain. These BMs are permeable at specific locations to allow the sensory axons to
607 enter the brain and use them as a substrate to grow towards the olfactory bulb, and at the same
608 time they maintain OP shape and position in the face of major morphogenetic movements
609 occuring during the brain flexure, and ensure proper separation of the two tissues by preventing
610 their intermixing.

611

612

613 **Material and Methods**

614

615 ***Zebrafish lines***

616 Wild-type, transgenic and mutant zebrafish embryos were obtained by natural spawning. In the
617 text, the developmental times in hpf indicate hours post-fertilization at 28°C. To obtain the 14-22
618 hpf stages, embryos were collected at 10 am, incubated for 2h at 28°C before being placed
619 overnight in a 23°C incubator to slow down development. Using this protocol, the embryos were
620 at 14 hpf in the following morning at 10 am. We used the following lines (the simplified names
621 are used in the figures and their legends): the zebrafish *sly*^{wi390} (*sly/lamc1*) mutant (referred to as
622 the *sly* mutant, Wiellette et al., 2004), the *foxd3*^{zdf10} mutant (referred to as the *foxd3* mutant,
623 Stewart et al., 2006), *Tg(-8.4neurog1:GFP)*^{sb1} (referred to as *Tg(neurog1:GFP)*, Blader et al.,
624 2003) to label the EONs at coalescence stages, *Tg(-2.0ompb:gapYFP)*^{rw032} (a gift from Nobuhiko
625 Miyasaka, RIKEN Institute, National Bioresource Project of Japan, referred to as
626 *Tg(omp:meYFP)*, Sato et al., 2007) to label *ompb*-expressing OP neurons and their axons from
627 22 hpf, *Tg(-4.0cldnb:GalTA4, cry:RFP)*^{nim11} (referred to as *Tg(cldnb:Gal4)*, Breau et al., 2013)
628 combined with *Tg(14XUAS:mRFP,Xla.Cryg:GFP)*^{tpl2} (referred to as *Tg(UAS:RFP),* Balciuniene
629 et al., 2013) to label all cells of the OP and their axons, *TgBAC(lamC1:lamC1-sfGFP)*
630 (Yamaguchi et al., 2022) to visualise the expression of LamC1-sfGFP under the control of the
631 *lamC1* promoter, and *Tg(eltC:GFP)*^{zf199Tg} (referred to as *Tg(elementC:gfp),* Stedman et al., 2009)
632 to label the forebrain. To generate the *Tg(UAS:lyn-tagRFP)* line, a *10XUAS:lyn-tagRFP* plasmid
633 was synthesized by Gateway cloning (final destination vector: pDest:tol2) and co-injected with
634 Tol2 mRNA (25 ng/µL of plasmid and 25 ng/µL of Tol2 mRNA) in 1 cell-stage wild type embryos.
635 All our experiments were made in agreement with the European Directive 210/63/EU on the
636 protection of animals used for scientific purposes, and the French application decree “Décret

637 2013-118". The fish facility has been approved by the French "Service for animal protection and
638 health", with the approval number B-75-05-25.
639
640 ***Genotyping***
641 The *sly*^{wi390} mutant allele and the wild type locus were genotyped by PCR with the following
642 primers: FW: 5'-CATGACGGCAAAGTTGGTGA-3'; RV1: 5'-CCATGCCTTGCAAAATGGCGTTA
643 CTTAA-3'; RV2: 5'-TGTAGGAGAGAAGTCGCGAG-3'. To detect the *sly*^{wi390} allele (which is an
644 insertion mutant allele, Wiellette et al., 2004), the FW and RV1 were used to amplify a PCR
645 product of 554 bp. The wild type allele was detected with the FW and RV2 primers to amplify a
646 PCR product of 617 bp. The *foxd3*^{zdf10} allele was genotyped with the CAPS (Cleaved Amplified
647 Polymorphic Sequences) technique (Neff et al., 2002) using the SspI restriction enzyme (NEB,
648 R132S), as described in Bryan et al., 2020.
649
650 ***Immunostainings***
651 For Laminin, Nidogen and Collagen IV immunostainings, embryos were fixed in 4%
652 paraformaldehyde (PFA, in PBS), dehydrated in methanol/PBS series and stored in methanol at
653 −20°C. Embryos were rehydrated in methanol/PBS series, washed in PBS and treated with 10
654 µg/mL proteinase K (embryos at 24 hpf or younger: 1 min 30 s of incubation, later stages: 3 min
655 of incubation). Embryos were then whashed in glycin 2 mg/mL, post-fixed in 4% PFA and
656 washed in PBS. For the other immunostainings, embryos were simply fixed in 4% PFA and
657 washed in PBS. Embryos were then blocked in 3% goat serum and 0.3% triton in PBS for 2h at
658 room temperature or overnight at 4°C and incubated overnight at 4°C with primary and
659 secondary antibodies.
660 The following primary antibodies were used: anti-Laminin (rabbit, 1/200, L-9393, Sigma), anti-
661 Nidogen (rabbit, 1/200, ab14511, Abcam), anti-Collagen IV (rabbit, 1/200, ab6586, Abcam), anti-
662 GFP (chicken, 1/200, GFP-1020, Aves labs), anti-DsRed (rabbit, 1/300, 632496, Takara), anti-
663 phospho-Histone H3 (rabbit, 1/200, 06-570, Millipore), anti-activated Caspase 3 (rabbit, 1/200,
664 AF835, R and D systems), anti-HuC/D (mouse, 1/200, clone 16A11, A-21271, Thermofischer
665 scientific) and anti-Dlx3b (mouse, 1/500, ZIRC).

666 ***In situ hybridisation***
667 Partial cDNA sequences for the NCC *crestin* marker were amplified by PCR using the 5'-
668 AAGCCCTCGAAACTCACCTG-3' (FW) and 5'-CCACTTGATTCCCACGAGCT-3' (RV) primers.
669 PCR products were subcloned in pGEM-T-easy (Promega) and sequenced. The

670 Digoxigenin(DIG)-labelled riboprobe was synthetized from PCR templates. Embryos were fixed
671 in 4% PFA in PBS and stored in methanol at −20 °C. Embryos were then rehydrated in
672 methanol/PBS series, permeabilized 1 min 30 s with proteinase K (10 mg/ml), pre-hybridized,
673 and hybridized overnight at 65 °C in hybridization mixture (50% formamide, 5 X standard saline
674 citrate (SSC), 0.1% Tween 20, 100 µg/ml heparin, 100 µg/ml tRNA in water). The embryos were
675 subjected to a series of washes in 50% SSC/formamide and SSC/PBST, and were then
676 incubated in the blocking solution (0.2% Tween 20, 0.2% Triton X-100, 2% sheep serum in
677 PBST) for one hour and overnight at 4 °C with alkaline phosphatase-conjugated anti-DIG
678 antibodies (Roche) diluted at 1/4000 in the blocking solution. Embryos were then washed in
679 PBST, soaked in staining buffer (TMN: 0,1M NaCl, 0,1M Tris-HCl, pH 9.5, 0.1% Tween 20 in
680 water) and incubated in NBT/BCIP (nitroblue tetrazolium/5-bromo-4-chloro-3-indolyl phosphate)
681 solution (Roche).
682
683 ***DNA injection***
684 To achieve mosaic labelling, the *-8.4neurog1:GFP* plasmid (Blader et al., 2003), the
685 *omp:meYFP* plasmid (Miyasaka et al., 2005) and the *sox10(7.2):KalTA4* plasmid (Almeida et al.,
686 2015) were injected respectively at 10, 5 and 15 ng/µL in 1-cell stage embryos.
687
688 ***Image acquisition***
689 For live imaging, embryos were dechorionated manually and mounted at 14 hpf in 0.5% low
690 melting agarose in 1X E3 medium. For movies on *Tg(neurog1:GFP)* embryos at coalescence
691 stages, the embryos were imaged directly after the mounting, using a dorsal view, from 14 to 22
692 hpf (or 14 to 32 hpf for embryos in which NCC were mosaically labelled). For movies on
693 *Tg(omp:meYFP)* embryos, the embryos were placed at 33°C just after the mounting, and
694 imaged from 22 hpf with a frontal view. Movies were recorded at 28°C on a Leica TCS SP8 MPII
695 upright multiphoton microscope using a 25X (numerical aperture (NA) 0.95) water lens. For fixed
696 embryos, immunostained embryos were mounted in 0.5% low melting agarose in PBS and
697 imaged on a Leica TCS SP5 AOBS upright confocal microscope using a 63X (NA 0.9) water
698 lens or on a Zeiss 980 FAST Airyscan with a 20X (NA 1.0) water lens.
699 For electron microscopy, the zebrafish embryos were fixed in 2% glutaraldehyde and 2% PFA in
700 0.1M sodium cacodylate buffer pH 7.2 overnight at 4°C. Samples were washed in 0.1M
701 cacodylate buffer, incubated for 1h in 1% osmium tetroxide in 0.1M cacodylate buffer, washed
702 with deionized water, incubated 1h in 1% Uranyl Acetate and washed again with deionized
703 water. To facilitate their orientation for sectionning, the zebrafish embryos were embedded in 4%

704 agarose before being dehydrated through graded concentration of ethanol (50-70-95-100%).
705 Samples were pre-embedded with graded concentration of anhydrous acetone and EPON
706 epoxy resin mix (3:1 – 1:1 – 1:3) and embedded with 100% EPON. Finally, the embryos were
707 mounted on silicon flat mold and polymerized at 60°C for 72 h. Ultrathin sections (80 nm) were
708 prepared with an Ultracut ultramicrotome (UCT, Leica microsystems). They were deposited on
709 silicon wafers, and contrasted with 2.5% uranyl acetate and 2% lead citrate. The wafers were
710 stuck on aluminum stubs, plasma-cleaned, and observed at 1.5 kV, with a 30 µm aperture
711 diameter and high current mode, at 2 mm WD, with SE and BSE in column detectors, in high
712 vacuum in a Field-Emission SEM (Gemini 500, Zeiss). Images were automatically acquired with
713 Atlas 5 (Fibics), with a pixel dwell time of 12.8 µs, a line averaging of 5, with a 8192 x 8192
714 definition and a pixel size fixed at 2.5 nm (corresponding to an image size of 20.5 × 20.5 µm),
715 and an overlap of 16% between images. To obtain final mosaics, LookUp Table were inverted,
716 SE and BSE signals were mixed, and manual stitching was made.

717 ***Image analysis***

718 *OP and brain dimensions.* The ML dimension of the OP represents the distance between the
719 most medial and the most lateral GFP+ or YFP+ cells in *Tg(neurog1:GFP)* or *Tg(omp:meYFP)*
720 embryos, respectively. Ectopic fluorescent cells (cells that are physically separated from the
721 main cluster) were not taken into account for this measurement. The same method was applied
722 to quantify the AP and DV dimensions of the OP tissue. The width of the brain was measured
723 along the ML axis using the GFP forebrain expression in *Tg(elementC:gfp)* embryos, at 3
724 different AP positions and 3 different DV positions.

725 *Thickness of the intercellular space in EM images.* Analyses were performed on 1000 pixel-long
726 rectangular regions at the interface between NCC and brain or OP cells in controls, and at the
727 brain/OP interface in *sly* mutants (from 3 to 7 regions per embryo). In each region, the thickness
728 of the intercellular space was manually measured every 100 pixels using Fiji (10
729 measurements/region). The average thickness per region and then per embryo was computed
730 and plotted.

731 *Manual cell tracking*. Individual cells from the OP (expressing *Tg(neurog1:GFP)* or
732 *Tg(omp:meYFP)*) and the adjacent brain were tracked in 3D using the Manual Tracking plugin in
733 ImageJ/Fiji. For tracking on *Tg(neurog1:GFP)* embryos, tracked cells from the brain and the OP
734 expressed *Tg(neurog1:GFP)* at least at the end of the movie. For tracking on *Tg(omp:meYFP)*
735 embryos, we followed forebrain cells located between the two OPs. For growth cone tracking,
736 individual growth cones were followed in 3D using the same plugin in embryos injected with the

omp:meYFP plasmid, over periods of 200 min each. The orientation of the trajectories represents the angle between the track and the vertical DV axis. 2D color coded trajectories and rose plots were generated in Matlab (Mathworks, US). The 3D MSD was computed using the Numpy library in Python (Harris et al., 2020). Plots representing cell tracks merged at their origin were produced with Microsoft Excel.

Segmentation and analysis of the brain/OP boundary. The segmentation of Dlx3b+ OP cells was performed using a two-step workflow in Ilastik and Fiji softwares. First, to achieve pixel classification, 3 representative images of controls and of *sly* mutants were loaded into the data input menu and used to train the algorithm. After the training the pixel features and feature size (sigma) were selected. All features on all sigma scales were selected. This allowed pixels to be classified based on gray intensity, resemblance to an edge, and texture. Next, the supervised training was performed. 3 examples of each object were labelled; then, the classifier was allowed to update to observe the results. Using the uncertainty overlay, areas of high uncertainty were labeled iteratively until the prediction layer showed satisfactory identification of the pixels. This process was repeated for all 3 images. The trained classifier was then run on all images, and the pixel classification data were saved as segmented images. In the second step, a “region of interest” (ROI) containing the brain/OP boundary was manually defined using Fiji. The edge detection was applied in that ROI and allowed the delineation of the boundary between segmented OP cells and brain cells. The data were exported as CSV files to be used for analysis. The distortion index is defined as the total length of the boundary, divided by the distance between the dorsalmost and ventralmost positions along the analysed boundary region.

Statistical analysis

Most graphs show means ± standard error of the mean (sem), overlayed with all individual data points. These plots were generated with the GraphPad Prism software. For all graphs, we checked for normality of the data distribution before performing parametric, unpaired, two tailed t tests. When the data were not normally distributed, a Mann-Whitney test was used. A Chi2 test was performed on the data presented in Fig. S2M-P and Fig. S4I-L. For the segmentation of the brain/OP boundary (Fig. 5G, H), the data were analyzed through an ANOVA test (mixed models, with animals as random effect and genotype and side as fixed effects). The orientation of cell and growth cone trajectories were treated as circular variables and analysed between groups using the circular analysis of variance based on the likelihood ratio test (Fig. 4O and Fig. 6C, F, I, L). The p values correspond to $*p < 0.05$, $**p < 0.01$, $***p < 0.001$. No statistical method was used to estimate sample size and no randomization was performed.

Acknowledgements

We gratefully acknowledge Isabelle Bonnet for her help in image analysis, and Alexis Eschstruth for his help in molecular biology. This work was funded by the Agence Nationale pour la Recherche (ANR-17-CE13-0009-01 NEUROMECHANICS and ANR-23-CE13-0025 MECAMATRIX), the Centre National pour la Recherche Scientifique (CNRS), Sorbonne Université, and the National Institute of Health NIDCD Grant R01-DC-017989. We also thank the imaging platform of the Institut de Biologie Paris-Seine (the facility is supported by CNRS, Sorbonne Université and the Conseil Régional Ile-de-France), and the IBPS aquatic platform for fish care.

781 **References**

782

783 **Abe, K., Baba, K., Huang, L., Wei, K. T., Okano, K., Hosokawa, Y. and Inagaki, N.** (2021).
784 Mechanosensitive axon outgrowth mediated by L1-laminin clutch interface. *Biophys J* **120**,
785 3566–3576.

786 **Aguillon, R., Madelaine, R., Aguirrebengoa, M., Guturu, H., Link, S., Dufourcq, P.,**
787 **Lecaudey, V., Bejerano, G., Blader, P. and Batut, J.** (2020). Morphogenesis is
788 transcriptionally coupled to neurogenesis during peripheral olfactory organ development.
789 *Development* **147**, (24): dev192971.

790 **Almeida, R.G. and Lyons, D.A.** (2015). Intersectional Gene Expression in Zebrafish Using the
791 Split KalTA4 System. *Zebrafish* **12**, 377-86.

792 **Anderson, C., Thorsteinsdóttir, S. and Borycki, A.G**. (2009). Sonic hedgehog-dependent
793 synthesis of laminin alpha1 controls basement membrane assembly in the myotome.
794 *Development* **136**, 3495-504.

795 **Balciuniene, J., Nagelberg, D., Walsh, K. T., Camerota, D., Georlette, D., Biemar, F.,**
796 **Bellipanni, G. and Balciunas, D.** (2013). Efficient disruption of Zebrafish genes using a Gal4-
797 containing gene trap. *BMC Genomics* **14**, 619.

798 **Baraban, M., Gordillo Pi, C., Bonnet, I., Gilles, J.-F., Lejeune, C., Cabrera, M., Tep, F. and**
799 **Breau, M. A.** (2023). Actomyosin contractility in olfactory placode neurons opens the skin
800 epithelium to form the zebrafish nostril. *Dev Cell* **58**, 361-375.e5.

801 **Belvindrah, R., Hankel, S., Walker, J., Patton, B. L. and Müller, U.** (2007). Beta1 integrins
802 control the formation of cell chains in the adult rostral migratory stream. *J Neurosci* **27**, 2704–
803 2717.

804 **Blader, P., Plessy, C. and Strahle, U.** (2003). Multiple regulatory elements with spatially and
805 temporally distinct activities control neurogenin1 expression in primary neurons of the zebrafish
806 embryo. *Mech Dev* **120**, 211–8.

807 **Bonner, J. and O'Connor, T. P.** (2001). The permissive cue laminin is essential for growth cone
808 turning in vivo. *J Neurosci* **21**, 9782–9791.

809 **Breau, M. A., Wilkinson, D. G. and Xu, Q.** (2013). A Hox gene controls lateral line cell
810 migration by regulating chemokine receptor expression downstream of Wnt signaling. *Proc Natl*
811 *Acad Sci U S A* **110**, 16892–16897.

812 **Breau, M. A., Bonnet, I., Stoufflet, J., Xie, J., De Castro, S. and Schneider-Maunoury, S.**
813 (2017). Extrinsic mechanical forces mediate retrograde axon extension in a developing neuronal
814 circuit. *Nat Commun* **8**, 282.

815 **Breau, M. A. and Trembleau, A**. (2023). Chemical and mechanical control of axon fasciculation
816 and defasciculation. *Semin Cell Dev Biol.* **140**, 72-81.
817 **Bryan, C. D., Chien, C. B. and Kwan, K. M.** (2016). Loss of laminin alpha 1 results in multiple
818 structural defects and divergent effects on adhesion during vertebrate optic cup morphogenesis.
819 *Dev Biol* **416**, 324–37.
820 **Bryan, C. D., Casey, M. A., Pfeiffer, R. L., Jones, B. W. and Kwan, K. M.** (2020). Optic cup
821 morphogenesis requires neural crest-mediated basement membrane assembly. *Development*
822 **147** (4): dev181420.
823 **Buisson, N., Sirour, C., Moreau, N., Denker, E., Le Bouffant, R., Goullancourt, A.,**
824 **Darribère, T. and Bello, V**. (2014). An adhesome comprising laminin, dystroglycan and myosin
825 IIA is required during notochord development in Xenopus laevis. *Development* **141**, 4569-79.
826 **Chang, J. and Chaudhuri, O.** (2019). Beyond proteases: Basement membrane mechanics and
827 cancer invasion. *J Cell Biol* **218**, 2456–2469.
828 **Chapman, S. C., Sawitzke, A. L., Campbell, D. S. and Schoenwolf, G. C.** (2005). A three-
829 dimensional atlas of pituitary gland development in the zebrafish. *J Comp Neurol* **487**, 428–440.
830 **Chen, Z.-L., Haegeli, V., Yu, H. and Strickland, S.** (2009). Cortical deficiency of laminin
831 gamma1 impairs the AKT/GSK-3beta signaling pathway and leads to defects in neurite
832 outgrowth and neuronal migration. *Dev Biol* **327**, 158–168.
833 **Crest, J., Diz-Muñoz, A., Chen, D. Y., Fletcher, D. A. and Bilder, D**. (2017) Organ sculpting by
834 patterned extracellular matrix stiffness. *Elife* **6**, e24958.
835 **Dang, P., Barnes, D. T., Cheng, R. P., Xu, A., Moon, Y. J., Kodukula, S. S. and Raper, J. A.**
836 (2023). Netrins and Netrin Receptors are Essential for Normal Targeting of Sensory Axons in the
837 Zebrafish Olfactory Bulb. *Neuroscience* **508**, 19–29.
838 **Díaz de la Loza, M. C., Díaz-Torres, A., Zurita, F., Rosales-Nieves, A. E., Moeendarbary, E.,**
839 **Franze, K., Martín-Bermudo, M. D. and González-Reyes, A.** (2017). Laminin Levels Regulate
840 Tissue Migration and Anterior-Posterior Polarity during Egg Morphogenesis in Drosophila. *Cell*
841 *Rep* **20**, 211–223.
842 **Dolez, M., Nicolas, J.-F. and Hirsinger, E.** (2011). Laminins, via heparan sulfate
843 proteoglycans, participate in zebrafish myotome morphogenesis by modulating the pattern of
844 Bmp responsiveness. *Development* **138**, 97–106.
845 **Dynes, J. L. and Ngai, J.** (1998). Pathfinding of olfactory neuron axons to stereotyped
846 glomerular targets revealed by dynamic imaging in living zebrafish embryos. *Neuron* **20**, 1081–
847 1091.
848 **Garcia, K. E., Okamoto, R. J., Bayly, P. V. and Taber, L. A.** (2017). Contraction and stress-

849 dependent growth shape the forebrain of the early chicken embryo. *J Mech Behav Biomed*
850 *Mater* **65**, 383–397.
851 **García-Alonso, L., Fetter, R. D. and Goodman, C. S.** (1996). Genetic analysis of Laminin A in
852 Drosophila: extracellular matrix containing laminin A is required for ocellar axon pathfinding.
853 *Development* **122**, 2611–2621.
854 **Grabham, P. W., Reznik, B. and Goldberg, D. J.** (2003). Microtubule and Rac 1-dependent F-
855 actin in growth cones. *J Cell Sci* **116**, 3739–3748.
856 **Grant, P. K. and Moens, C. B.** (2010). The neuroepithelial basement membrane serves as a
857 boundary and a substrate for neuron migration in the zebrafish hindbrain. *Neural Dev* **5**, 9.
858 **Harden, M. V., Pereiro, L., Ramialison, M., Wittbrodt, J., Prasad, M. K., McCallion, A. S. and**
859 **Whitlock, K. E.** (2012). Close association of olfactory placode precursors and cranial neural
860 crest cells does not predestine cell mixing. *Dev Dyn* **241**, 1143–54.
861 **Harmansa, S., Erlich, A., Eloy, C., Zurlo, G. and Lecuit, T.** (2023). Growth anisotropy of the
862 extracellular matrix shapes a developing organ. *Nat Commun* **14**, 1220.
863 **Harris, C. R., Millman, K. J., van der Walt, S. J., Gommers, R., Virtanen, P., Cournapeau,**
864 **D., Wieser, E., Taylor, J., Berg, S., Smith, N. J., et al.** (2020). Array programming with NumPy.
865 *Nature* **585**, 357–362.
866 **Harunaga, J. S., Doyle, A. D. and Yamada, K. M.** (2014). Local and global dynamics of the
867 basement membrane during branching morphogenesis require protease activity and actomyosin
868 contractility. *Dev Biol* **394**, 197–205.
869 **Hauptmann, G. and Gerster, T.** (2000). Regulatory gene expression patterns reveal transverse
870 and longitudinal subdivisions of the embryonic zebrafish forebrain. *Mech Dev* **91**, 105–118.
871 **Höpker, V. H., Shewan, D., Tessier-Lavigne, M., Poo, M. and Holt, C.** (1999). Growth-cone
872 attraction to netrin-1 is converted to repulsion by laminin-1. *Nature* **401**, 69–73.
873 **Huang, C.-C., Hall, D. H., Hedgecock, E. M., Kao, G., Karantza, V., Vogel, B. E., Hutter, H.,**
874 **Chisholm, A. D., Yurchenco, P. D. and Wadsworth, W. G.** (2003). Laminin alpha subunits and
875 their role in C. elegans development. *Development* **130**, 3343–3358.
876 **Ihara, S., Hagedorn, E. J., Morrissey, M. A., Chi, Q., Motegi, F., Kramer, J. M. and**
877 **Sherwood, D. R.** (2011). Basement membrane sliding and targeted adhesion remodels tissue
878 boundaries during uterine-vulval attachment in Caenorhabditis elegans. *Nat Cell Biol* **13**, 641–
879 651.
880 **Ivanovitch, K., Cavodeassi, F. and Wilson, S. W.** (2013). Precocious acquisition of
881 neuroepithelial character in the eye field underlies the onset of eye morphogenesis. *Dev Cell* **27**,
882 293–305.

883 **Kafitz, K. W. and Greer, C. A.** (1997). Role of laminin in axonal extension from olfactory
884 receptor cells. *J Neurobiol* **32**, 298–310.
885 **Karamanos, N. K., Piperigkou, Z., Passi, A., Götte, M., Rousselle, P. and Vlodavsky, I.**
886 (2021). Extracellular matrix-based cancer targeting. *Trends Mol Med* **27**, 1000–1013.
887 **Karlstrom, R. O., Trowe, T., Klostermann, S., Baier, H., Brand, M., Crawford, A. D.,**
888 **Grunewald, B., Haffter, P., Hoffmann, H., Meyer, S. U., et al.** (1996). Zebrafish mutations
889 affecting retinotectal axon pathfinding. *Development* **123**, 427–438.
890 **Kaur, S., Kaur, I., Rawal, P., Tripathi, D. M. and Vasudevan, A.** (2021). Non-matrigel scaffolds
891 for organoid cultures. *Cancer Lett* **504**, 58–66.
892 **Khalilgharibi, N. and Mao, Y**. (2021). To form and function: on the role of basement membrane
893 mechanics in tissue development, homeostasis and disease. *Open Biol* **11**, 200360.
894 **Kim, S., Uroz, M., Bays, J. L. and Chen, C. S.** (2021). Harnessing Mechanobiology for Tissue
895 Engineering. *Dev Cell* **56**, 180–191.
896 **Lakhina, V., Marcaccio, C. L., Shao, X., Lush, M. E., Jain, R. A., Fujimoto, E., Bonkowsky,**
897 **J. L., Granato, M. and Raper, J. A.** (2012). Netrin/DCC signaling guides olfactory sensory
898 axons to their correct location in the olfactory bulb. *J Neurosci* **32**, 4440–4456.
899 **Lee, J. and Gross, J. M.** (2007). Laminin beta1 and gamma1 containing laminins are essential
900 for basement membrane integrity in the zebrafish eye. *Invest Ophthalmol Vis Sci* **48**, 2483–
901 2490.
902 **Li, S., Liquari, P., McKee, K. K., Harrison, D., Patel, R., Lee, S. and Yurchenco, P. D.** (2005).
903 Laminin-sulfatide binding initiates basement membrane assembly and enables receptor
904 signaling in Schwann cells and fibroblasts. *J Cell Biol* **169**, 179–189.
905 **Loganathan, R., Rongish, B. J., Smith, C. M., Filla, M. B., Czirok, A., Bénazéraf, B. and**
906 **Little, C. D.** (2016). Extracellular matrix motion and early morphogenesis. *Development* **143**,
907 2056–2065.
908 **Luo, R., An, M., Arduini, B. L. and Henion, P. D**. (2001) Specific pan-neural crest expression
909 of zebrafish Crestin throughout embryonic development. *Dev Dyn* **220**, 69-74.
910 **Madelaine, R., Garric, L. and Blader, P.** (2011). Partially redundant proneural function reveals
911 the importance of timing during zebrafish olfactory neurogenesis. *Development* **138**, 4753–62.
912 **Miner, J. H. and Yurchenco, P. D.** (2004). Laminin functions in tissue morphogenesis. *Annu*
913 *Rev Cell Dev Biol* **20**, 255–284.
914 **Miyasaka, N., Sato, Y., Yeo, S.-Y., Hutson, L. D., Chien, C.-B., Okamoto, H. and Yoshihara,**
915 **Y.** (2005). Robo2 is required for establishment of a precise glomerular map in the zebrafish
916 olfactory system. *Development* **132**, 1283–1293.

917 **Miyasaka, N., Knaut, H. and Yoshihara, Y.** (2007). Cxcl12/Cxcr4 chemokine signaling is
918 required for placode assembly and sensory axon pathfinding in the zebrafish olfactory system.
919 *Development* **134**, 2459–2468.
920 **Monnot, P., Gangatharan, G., Baraban, M., Pottin, K., Cabrera, M., Bonnet, I. and Breau, M.
921 A.** (2022). Intertissue mechanical interactions shape the olfactory circuit in zebrafish. *EMBO Rep*
922 **23**, e52963.
923 **Moore, R. E., Pop, S., Alleyne, C. and Clarke, J. D. W.** (2022). Microtubules are not required
924 to generate a nascent axon in embryonic spinal neurons in vivo. *EMBO reports* **23**, e52493.
925 **Nazari, S. S., Doyle, A. D. and Yamada, K. M.** (2022). Mechanisms of Basement Membrane
926 Micro-Perforation during Cancer Cell Invasion into a 3D Collagen Gel. *Gels* **8**, 567.
927 **Neff, M. M., Turk, E. and Kalishman, M.** (2002). Web-based primer design for single nucleotide
928 polymorphism analysis. *Trends Genet* **18**, 613–615.
929 **Nguyen-Ba-Charvet, K. T., Brose, K., Marillat, V., Sotelo, C., Tessier-Lavigne, M. and
930 Chédotal, A.** (2001). Sensory axon response to substrate-bound Slit2 is modulated by laminin
931 and cyclic GMP. *Mol Cell Neurosci* **17**, 1048–1058.
932 **Odenthal, J., Haffter, P., Vogelsang, E., Brand, M., van Eeden, F. J., Furutani-Seiki, M.,
933 Granato, M., Hammerschmidt, M., Heisenberg, C. P., Jiang, Y. J., et al.** (1996). Mutations
934 affecting the formation of the notochord in the zebrafish, Danio rerio. *Development* **123**, 103–
935 115.
936 **Parsons, M. J., Pollard, S. M., Saúde, L., Feldman, B., Coutinho, P., Hirst, E. M. A. and
937 Stemple, D. L.** (2002). Zebrafish mutants identify an essential role for laminins in notochord
938 formation. *Development* **129**, 3137–3146.
939 **Pastor-Pareja, J. C. and Xu, T.** (2011). Shaping Cells and Organs in Drosophila by Opposing
940 Roles of Fat Body-Secreted Collagen IV and Perlecan. *Developmental Cell* **21**, 245–256.
941 **Paulus, J. D. and Halloran, M. C.** (2006). Zebrafish bashful/laminin-alpha 1 mutants exhibit
942 multiple axon guidance defects. *Dev Dyn* **235**, 213–224.
943 **Pollard, S. M., Parsons, M. J., Kamei, M., Kettleborough, R. N. W., Thomas, K. A., Pham, V.
944 N., Bae, M.-K., Scott, A., Weinstein, B. M. and Stemple, D. L.** (2006). Essential and
945 overlapping roles for laminin alpha chains in notochord and blood vessel formation. *Dev Biol*
946 **289**, 64–76.
947 **Powell, S. K. and Kleinman, H. K.** (1997). Neuronal laminins and their cellular receptors. *Int J
948 Biochem Cell Biol* **29**, 401–414.
949 **Randlett, O., Poggi, L., Zolessi, F. R. and Harris, W. A.** (2011). The oriented emergence of
950 axons from retinal ganglion cells is directed by laminin contact in vivo. *Neuron* **70**, 266–280.

951 **Ross, L. S., Parrett, T. and Easter, S. S.** (1992). Axonogenesis and morphogenesis in the
952 embryonic zebrafish brain. *J Neurosci* **12**, 467–482.
953 **Sato, Y., Miyasaka, N. and Yoshihara, Y.** (2005). Mutually exclusive glomerular innervation by
954 two distinct types of olfactory sensory neurons revealed in transgenic zebrafish. *J Neurosci* **25**,
955 4889–4897.
956 **Sato, Y., Miyasaka, N. and Yoshihara, Y.** (2007). Hierarchical regulation of odorant receptor
957 gene choice and subsequent axonal projection of olfactory sensory neurons in zebrafish. *J*
958 *Neurosci* **27**, 1606–1615.
959 **Semina, E. V., Bosenko, D. V., Zinkevich, N. C., Soules, K. A., Hyde, D. R., Vihtelic, T. S.,**
960 **Willer, G. B., Gregg, R. G. and Link, B. A.** (2006). Mutations in laminin alpha 1 result in
961 complex, lens-independent ocular phenotypes in zebrafish. *Dev Biol* **299**, 63–77.
962 **Serna-Morales, E., Sánchez-Sánchez, B.J., Marcotti, S., Nichols, A., Bhargava, A., Dragu,**
963 **A., Hirvonen, L.M., Díaz-de-la-Loza, M.D., Mink, M., Cox, S., Rayfield, E., Lee, R.M.,**
964 **Hobson, C.M., Chew, T.L. and Stramer, B.M**. (2023) Extracellular matrix assembly stress
965 initiates Drosophila central nervous system morphogenesis. *Dev Cell* **58**, 825-835.e6.
966 **Shay, E. L., Greer, C. A. and Treloar, H. B.** (2008). Dynamic expression patterns of ECM
967 molecules in the developing mouse olfactory pathway. *Dev Dyn* **237**, 1837–1850.
968 **Sidhaye, J. and Norden, C.** (2017). Concerted action of neuroepithelial basal shrinkage and
969 active epithelial migration ensures efficient optic cup morphogenesis. *Elife* **6**,.
970 **Sittaramane, V., Sawant, A., Wolman, M. A., Maves, L., Halloran, M. C. and Chandrasekhar,**
971 **A.** (2009). The cell adhesion molecule Tag1, transmembrane protein Stbm/Vangl2, and
972 Lamininalpha1 exhibit genetic interactions during migration of facial branchiomotor neurons in
973 zebrafish. *Dev Biol* **325**, 363–373.
974 **Smyth, N., Vatansever, H. S., Murray, P., Meyer, M., Frie, C., Paulsson, M. and Edgar, D.**
975 (1999). Absence of basement membranes after targeting the LAMC1 gene results in embryonic
976 lethality due to failure of endoderm differentiation. *J Cell Biol* **144**, 151–160.
977 **Soleman, S., Filippov, M. A., Dityatev, A. and Fawcett, J. W.** (2013). Targeting the neural
978 extracellular matrix in neurological disorders. *Neuroscience* **253**, 194–213.
979 **Stedman, A., Lecaudey, V., Havis, E., Anselme, I., Wassef, M., Gilardi-Hebenstreit, P. and**
980 **Schneider-Maunoury, S.** (2009). A functional interaction between Irx and Meis patterns the
981 anterior hindbrain and activates krox20 expression in rhombomere 3. *Dev Biol* **327**, 566–577.
982 **Stemple, D. L., Solnica-Krezel, L., Zwartkruis, F., Neuhauss, S. C., Schier, A. F., Malicki, J.,**
983 **Stainier, D. Y., Abdelilah, S., Rangini, Z., Mountcastle-Shah, E., et al.** (1996). Mutations
984 affecting development of the notochord in zebrafish. *Development* **123**, 117–128.

985 **Stewart, R. A., Arduini, B. L., Berghmans, S., George, R. E., Kanki, J. P., Henion, P. D. and**
986 **Look, A. T.** (2006). Zebrafish foxd3 is selectively required for neural crest specification,
987 migration and survival. *Developmental Biology* **292**, 174–188.
988 **Suter, T. and Jaworski, A.** (2019). Cell migration and axon guidance at the border between
989 central and peripheral nervous system. *Science* **365**,.
990 **Theocharis, A. D., Manou, D. and Karamanos, N. K.** (2019). The extracellular matrix as a
991 multitasking player in disease. *FEBS J* **286**, 2830–2869.
992 **Töpfer, U., Guerra Santillán, K. Y., Fischer-Friedrich, E. and Dahmann, C.** (2022). Distinct
993 contributions of ECM proteins to basement membrane mechanical properties in Drosophila.
994 *Development* **149**, dev200456.
995 **Torres-Paz, J. and Whitlock, K. E.** (2014). Olfactory sensory system develops from
996 coordinated movements within the neural plate. *Dev Dyn* **243**, 1619–31.
997 **Torres-Paz, J., Tine, E. M. and Whitlock, K. E.** (2021). Dissecting the neural divide: a
998 continuous neurectoderm gives rise to the olfactory placode and bulb. *Int J Dev Biol* **65**, 275–
999 287.
1000 **Tropepe, V. and Sive, H. L.** (2003). Can zebrafish be used as a model to study the
1001 neurodevelopmental causes of autism? *Genes Brain Behav* **2**, 268–281.
1002 **Tsuda, S., Kitagawa, T., Takashima, S., Asakawa, S., Shimizu, N., Mitani, H., Shima, A.,**
1003 **Tsutsumi, M., Hori, H., Naruse, K., et al.** (2010). FAK-mediated extracellular signals are
1004 essential for interkinetic nuclear migration and planar divisions in the neuroepithelium. *J Cell Sci*
1005 **123**, 484–496.
1006 **Urbano, J. M., Torgler, C. N., Molnar, C., Tepass, U., López-Varea, A., Brown, N. H., de**
1007 **Celis, J. F. and Martín-Bermudo, M. D.** (2009). Drosophila laminins act as key regulators of
1008 basement membrane assembly and morphogenesis. *Development* **136**, 4165–4176.
1009 **Van De Bor, V., Loreau, V., Malbouyres, M., Cerezo, D., Placenti, A., Ruggiero, F. and**
1010 **Noselli, S.** (2021). A dynamic and mosaic basement membrane controls cell intercalation in
1011 Drosophila ovaries. *Development* **148**,.
1012 **Vöcking, O., Van Der Meulen, K., Patel, M. K. and Famulski, J. K.** (2023). Zebrafish anterior
1013 segment mesenchyme progenitors are defined by function of tfap2a but not sox10.
1014 *Differentiation* **130**, 32–42.
1015 **Walma, D. A. C. and Yamada, K. M.** (2020). The extracellular matrix in development.
1016 *Development* **147**, dev175596.
1017 **Weinl, C., Drescher, U., Lang, S., Bonhoeffer, F. and Löschinger, J.** (2003). On the turning of
1018 Xenopus retinal axons induced by ephrin-A5. *Development* **130**, 1635–1643.

1019 **Whitlock, K. E. and Westerfield, M.** (1998). A transient population of neurons pioneers the
1020 olfactory pathway in the zebrafish. *J Neurosci* **18**, 8919–8927.
1021 **Whitlock, K. E. and Westerfield, M.** (2000). The olfactory placodes of the zebrafish form by
1022 convergence of cellular fields at the edge of the neural plate. *Development* **127**, 3645–53.
1023 **Wiellette, E., Grinblat, Y., Austen, M., Hirsinger, E., Amsterdam, A., Walker, C.,**
1024 **Westerfield, M. and Sive, H.** (2004). Combined haploid and insertional mutation screen in the
1025 zebrafish. *Genesis* **40**, 231–240.
1026 **Wolman, M. A., Sittaramane, V. K., Essner, J. J., Yost, H. J., Chandrasekhar, A. and**
1027 **Halloran, M. C.** (2008). Transient axonal glycoprotein-1 (TAG-1) and laminin-alpha1 regulate
1028 dynamic growth cone behaviors and initial axon direction in vivo. *Neural Dev* **3**, 6.
1029 **Yamada, K. M., Doyle, A. D. and Lu, J.** (2022). Cell-3D matrix interactions: recent advances
1030 and opportunities. *Trends Cell Biol* **32**, 883–895.
1031 **Yamaguchi, N., Zhang, Z., Schneider, T., Wang, B., Panozzo, D. and Knaut, H.** (2022). Rear
1032 traction forces drive adherent tissue migration in vivo. *Nat Cell Biol* **24**, 194–204.
1033 **Zamir, E. A., Rongish, B. J. and Little, C. D.** (2008). The ECM moves during primitive streak
1034 formation--computation of ECM versus cellular motion. *PLoS Biol* **6**, e247.
1035
1036

1037 **Figure legends**

1038

1039 **Figure 1. Expression profile of Laminin in relation with the development of the olfactory**
1040 **system. A-D.** Immunostaining for Laminin (magenta) on *Tg(neurog1:GFP)* embryos (green) at
1041 18 and 22 hpf (A-B', dorsal views), and on *Tg(omp:meYFP)* embryos (green) at 28 and 36 hpf
1042 (C-D', frontal views). In A, white arrowheads = BM-like Laminin staining around the brain, grey
1043 arrowheads = spotty Laminin accumulation around the OP. In C, D, asterisks = interruptions in
1044 the OP's and brain's BM where the YFP+ axons exit the OP and enter the brain. arrows =
1045 distalmost extremity of the YFP+ axon bundle, which is in close contact with the internal side of
1046 the brain's BM. In C', D', white arrowheads = ventro-medial unipolar neurons labelled by the
1047 *Tg(omp:meYFP)* line (see Miyasaka et al., 2005). All the images are single z-sections. **E-J.**
1048 Images extracted from confocal live imaging on *TgBAC(lamC1:lamC1-sfGFP); Tg(cldnb:Gal4;*
1049 *UAS:RFP)* embryos (frontal view, except for Fig. 1J, dorsal view). LamC1-sfGFP expression in
1050 green, and RFP expression (OP cells and peridermal skin cells) in magenta. Arrowheads = OP
1051 cells with cytoplasmic LamC1-sfGFP accumulation. Asterisks in F and H = axon exit point and
1052 entry point, respectively. Arrows in H and I = distalmost extremity of the RFP+ axon bundle,
1053 located close to the brain's BM. In J, double headed arrow = gap in the LamC1-sfGFP observed
1054 at the interface with the periderm, where the nostril orifice opens in the skin, as previously
1055 reported (Baraban et al., 2023). All the images are single z-sections**. K.** Schematic
1056 representation of Laminin-containing BM (magenta) assembly during OP coalescence (a, b), of
1057 the formation of the exit/entry points, which often appear as zones with several, small BM
1058 interruptions (b, d) and the associated axonal behaviours: retrograde axon extension and lateral
1059 movement in the OP (a, b, grey arrows), growth as a fasciculated bundle, initially between the
1060 BMs of the OP and the brain (c), and then migration of the axonal tips along the internal side of
1061 the brain's BM (d). Scale bar: 50 µm.

1062

1063 **Figure 2. The integrity of the BMs of OP and brain tissues is strongly affected in *sly***
1064 **mutants. A-I.** Immunostaining for Laminin (A-C), Nidogen (D-F) and Collagen IV (G-I) (magenta)
1065 on *sly* mutants and control siblings at 22 (dorsal view), 28, and 36 hpf (frontal view). For Laminin
1066 and Nidogen, the linear, BM-like staining seen in controls around the OP and brain tissues is not
1067 detected in *sly* mutants. In G, white arrowheads = BM-like linear Collagen IV staining, grey
1068 arrowheads = fibrous staining around the OP. In *sly* mutants, the linear Collagen IV pattern is
1069 dramatically disrupted, with, however, remaining fibrous patches of Collagen IV in some discrete
1070 areas located at the margin of the OP and/or between the OP and brain (arrows in G', H', I').

1071 Scale bar: 50 µm. **J, K**. Examples of EM images of the intercellular space between NCC and the
1072 OP in control siblings (J, K) and the OP and the brain in *sly* mutants (J', K'), at 24 (J, J') and 32
1073 hpf (K, K'). Arrows = plasma membranes. The pictures were taken in the areas depicted with red
1074 boxes in L, L'. **L.** Schematic view of the brain/OP boundary and of the areas (red boxes) where
1075 the pictures were taken in controls (L) and *sly* mutants (L'). OP, brain and NCC were identified
1076 by their position and shape: migrating NCC showed an elongated morphology along the AP axis,
1077 which differed from the round OP cell bodies and from brain neuroepithelial cells elongated
1078 along the ML axis. **M, N.** Thickness of the intercellular space in *sly* mutants (between OP and
1079 brain cells) and control siblings (between NCC and brain or OP cells) at 24 hpf (n = 3 controls; n
1080 = 3 mutants) and 32 hpf (n = 2 controls; n = 3 mutants). For 24 hpf, unpaired, two-tailed t test.
1081 For 32 hpf, Mann-Whitney test.
1082
1083 **Figure 3. Analysis of OP coalescence in *sly* mutants and control siblings. A, B.** Images
1084 (dorsal views, 1 z-section) of representative OPs from a *Tg(neurog1:GFP); sly* $^{-/-}$ mutant (right)
1085 and a control *Tg(neurog1:GFP)* sibling (left) at the end of OP coalescence (22 hpf). The
1086 *Tg(neurog1:GFP)*$^{+}$ OP clusters are surrounded by dotted lines. **C-E.** Graphs showing the
1087 anteroposterior (AP, in C), the mediolateral (ML, in D), and dorsoventral (DV, in E) dimensions of
1088 the *Tg(neurog1:GFP)*$^{+}$ OP clusters in *sly* mutants (pink) and control siblings (blue) at 22 hpf (n =
1089 62 controls and n = 32 mutants from 2 independent experiments). Ectopic fluorescent cells (cells
1090 that are physically separated from the main cluster) were not taken into account for the
1091 measurement of OP dimensions. Unpaired, two-tailed t test. **F-F'' and H-H''.** Images extracted
1092 from confocal live imaging on *Tg(neurog1:GFP)* control (F-F'') and *sly* mutant (H-H'') embryos
1093 during OP coalescence, dorsal view, average projection. Only the left side of the embryo is
1094 shown. **G, I.** Examples of 2D tracks (ML along X and AP along Y) of *Tg(neurog1:GFP)*$^{+}$ OP cells
1095 (red) and *Tg(neurog1:GFP)*$^{+}$ brain cells (green) in a control (G) and a *sly* mutant embryo (I).
1096 Only the left side of the embryo is shown. The time is color-coded: light colors at the beginning
1097 of the trajectory (17 hpf) towards dark colors for the end of the track (600 min later). **J, K.** MSD
1098 analysis for OP cells (J) and brain cells (K) in *sly* mutants and control siblings (n = 5 controls and
1099 n = 5 mutants from 3 independent experiments, 10 to 14 cells analysed in each tissue). **L, M.**
1100 Graphs showing the total lateral (L) and ventral (M) displacement of OP cells, starting at 17 hpf
1101 and during 600 min of time lapse (n = 5 control placodes and n = 5 mutant placodes from 3
1102 independent experiments, 10 to 14 cells per placode, unpaired, two-tailed t test). **N-P.** Graphs
1103 showing the total anterior displacement of anterior, central and posterior OP cells (as defined in
1104 Breau et al., 2017), starting at 17 hpf and during 600 min of time lapse (n = 5 control placodes

1105 and n = 5 mutant placodes from 3 independent experiments, mean calculated from 1 to 12 cells
1106 per placode, unpaired, two-tailed t test). Note that in some of the OPs we could not find any
1107 trackable (i.e. expressing H2B-RFP) posterior OP cell, which explains why there are only 4
1108 control points and 3 mutant points in the graph showing the anterior displacement of posterior
1109 cells).
1110
1111 **Figure 4. Analysis of OP and brain morphogenesis in *sly* mutants and control siblings**
1112 **during the forebrain flexure. A, B.** Images (frontal view, 1 z-section) of representative
1113 placodes from a *Tg(omp:meYFP); sly* $^{-/-}$ mutant (right) and a control *Tg(omp:meYFP)* sibling (left)
1114 at 36 hpf. Laminin immunostaining in magenta. **C-E.** Graphs showing the anteroposterior (AP, in
1115 C), the mediolateral (ML, in D), and dorsoventral (DV, in E) dimensions of the *Tg(omp:meYFP)*$^{+}$
1116 OP clusters in *sly* mutants (pink) and control siblings (blue) at 36 hpf (n = 15 controls and n = 9
1117 mutants from 4 independent experiments). Ectopic fluorescent cells (cells that are physically
1118 separated from the main cluster) were not taken into account for the measurement of OP
1119 dimensions. Unpaired, two-tailed t test. Similar measurements performed at younger stages are
1120 shown in Fig. S3A-L. **F, G.** Examples of images used for the analysis of ectopic cells, defined as
1121 *Tg(omp:meYFP)*+ cells being physically separated from the main YFP+ cluster. Arrowheads
1122 show instances of ectopic cells in a *sly* mutant. **H.** Table showing the % of control and mutant
1123 embryos with at least one ectopic cell located dorsally, ventrally, laterally, and medially to the
1124 main YFP+ cluster. The numbers of analysed embryos are indicated in the table. **I-I'' and K-K''.**
1125 Images extracted from confocal live imaging on *Tg(omp:meYFP)* control (I-I'') and *sly* mutant (K-
1126 K'') embryos during the forebrain flexure, from 22 hpf and over 1080 min, frontal view, maximum
1127 projection. Only the left side of the embryo is shown. **J, L.** Examples of 2D tracks (ML along X
1128 and DV along Y) of *Tg(omp:meYFP)*$^{+}$ OP cells (red) and adjacent brain cells (green) in a control
1129 (J) and a *sly* mutant (L). The time is color-coded: light colors at the beginning of the trajectory
1130 (22 hpf) towards dark colors for the end of the track (1080 min later). Only the left side of the
1131 embryo is shown**. M, N.** 3D MSD analysis of OP (M) and brain cells (N) in *sly* mutants and
1132 control siblings (n = 4 controls and n = 3 mutants from 5 independent experiments, 10 to 14 cells
1133 analysed in each tissue). **O.** Rose plots indicating the orientation of the movement for control
1134 and mutant left OP cells (data pooled from n = 4 controls and n = 3 mutants from 5 independent
1135 experiments). Numbers = number of cells. Dorsal to the top, lateral to the left. There is a
1136 statistical difference in cell track orientations between controls and mutants (circular analysis of
1137 variance based on the likelihood ratio test: p = 1.233e-09 for the left OPs, and p = 3.439e-08 for
1138 the right OPs, the graphs for the rigth OPs are not shown).

1139

1140 **Figure 5. Analysis of brain width and brain/placode boundary in *sly* mutants and control**
1141 **siblings. A, A'.** Immunostaining for HuC (cyan) at 36 hpf on *Tg(cldnb:Gal4; UAS:RFP)*
1142 (magenta) control and *sly* mutant embryos (frontal view). Similar immunostainings performed at
1143 28 hpf are shown in Fig. S4A, A'. **B, B'**. Images of *Tg(elementC:gfp); Tg(cldnb:Gal4; UAS:RFP)*
1144 control and mutant embryos at 36 hpf (frontal view), similar images acquired at 28 hpf are shown
1145 in Fig. S4B, B'. GFP (green) is expressed by the forebrain and a few OP cells. Arrows indicate
1146 where the brain width was measured (in 3 distinct positions along the DV axis). Measurements
1147 were also carried out at 3 distinct AP levels (through the z-stack). **C, D.** Width of the forebrain in
1148 36 hpf controls and *sly* mutants, at 3 different DV and 3 different AP levels (n = 9 controls and n
1149 = 8 mutants from 4 independent experiments, unpaired, two-tailed t test). Quantifications for the
1150 28 hpf stage are shown in Fig. S4C, D. **E-F'.** Immunostaining for the OP marker Dlx3b (cyan)
1151 was performed on 36 hpf *sly* mutants and control siblings (frontal view). The signal was
1152 segmented using deep learning approaches (white signal), and the distortion index (see Material
1153 and Methods) of the OP/brain boundary was calculated in the regions outlined with red boxes.
1154 **G, H.** Graphs showing the distortion indexes in controls and mutants at 36 hpf, for the left and
1155 right OPs (n = 3 controls and n = 3 mutants). ANOVA test (mixed models, with animals as
1156 random effect and genotype and side as fixed effects).

1157

1158 **Figure 6. Quantitative live imaging of axonal behaviours in *sly* mutants and control**
1159 **siblings. A, B.** Images extracted from confocal live imaging on control (A-A'''') and *sly* mutant
1160 (B-B'''') embryos injected with the *omp:meYFP* plasmid to obtain a mosaic labelling of OP
1161 neurons and their axons (frontal view, maximum projections). The OP neurons and their axons
1162 were imaged every 10 min over 1000 min from 22 hpf. Here, only the 200-400 min time window
1163 is shown as an example. Arrowheads = positions of individual growth cones over time. **C-N**.
1164 Individual YFP+ growth cones, as well as YFP+ cell bodies in the OP, were tracked during 4
1165 consecutive periods of 200 min each (from 200 min of imaging, since before no growth cone
1166 could be detected, n = 5 mutants and n = 5 controls from 6 independent experiments). The
1167 mean movement of OP cell bodies was substracted from the growth cone tracks to get rid of the
1168 global flexure movement. 200-400 min: 6 growth cones in controls, 4 in mutants; 400-600 min:
1169 15 growth cones in controls, 4 in mutants; 600-800 min: 18 growth cones in controls, 4 in
1170 mutants; 800-1000 min: 16 growth cones in controls, 7 in mutants. **C, F, I, L**. Tracks of the
1171 growth cones merged at their origin for the 4 consecutive periods of 200 min. For each time
1172 window, the difference in the orientation of the tracks was analysed using the circular analysis of

1173 variance based on the likelihood ratio test. **D, G, J, M.** Mean speed of the growth cones.
1174 Unpaired, two-tailed t tests. **E, H, K, N.** Persistence of the growth cones, defined as the distance
1175 between the initial and final positions of the growth cones divided by the total length of their
1176 trajectory. Unpaired, two-tailed t tests, except for the analysis of the persistence at 400-600 min,
1177 and for the speed and persistence at 600-800 min, where Mann Whitney tests were performed.
1178
1179 **Figure S1. Electron microscopy analysis of intercellular spaces in the OP and brain**
1180 **tissues. A, A' and C, C'.** Examples of images of the intercellular space located between OP
1181 cells in control siblings (A, C) and in *sly* mutants (A', C'), at 24 and 32 hpf. Arrows = plasma
1182 membranes. **B, D.** Thickness of the intercellular space in the OP tissue in *sly* mutants and
1183 control siblings at 24 (n = 3 controls; n = 3 mutants) and 32 hpf (n = 2 controls; n = 3 mutants).
1184 Unpaired, two-tailed t test. **E, E' and G, G'.** Examples of images of the intercellular space
1185 located between brain cells in control siblings (A, C) and in *sly* mutants (A', C'), at 24 and 32 hpf.
1186 Arrows = plasma membranes. **F, H.** Thickness of the intercellular space in the brain tissue in *sly*
1187 mutants and control siblings at 24 (n = 3 controls; n = 3 mutants) and 32 hpf (n = 2 controls; n =
1188 3 mutants). Unpaired, two-tailed t test.
1189
1190 **Figure S2. Analysis of proliferation and apoptosis in the OPs of *sly* mutants and control**
1191 **siblings. A-D'.** Immunostaining for Phospho-histone H3 (magenta) to label dividing cells on
1192 *Tg(neurog1:GFP)* embryos (green) at 16 hpf and 21 hpf (A-B' show images at 21 hpf, dorsal
1193 view), and on *Tg(omp:meYFP)* embryos (green) at 28 and 36 hpf (C-D' show images at 36 hpf,
1194 frontal view). In A-B' the OP is surrounded by a dotted line. Arrows = instances of Phospho-
1195 histone H3 positive cells in the placodal *Tg(neurog1:GFP)+ or Tg(omp:meYFP)+* clusters. **E-H.**
1196 Number of Phospho-histone H3 positive cells in the OP at 16, 21, 28 and 36 hpf in control
1197 embryos and *sly* mutants. Unpaired, two-tailed t test. **I-L'.** Immunostaining for Activated Caspase
1198 3 (magenta) to label apoptotic cells/debris on *Tg(neurog1:GFP)* embryos (green) at 16 hpf and
1199 21 hpf (I-J' show images at 21 hpf, dorsal view), and on *Tg(omp:meYFP)* embryos (green) at 28
1200 and 36 hpf (K-L' show images at 36 hpf, frontal view). In I-J' the OP is surrounded by a dotted
1201 line. Arrows = instances of Activated Caspase 3 positive cells or debris in the OP or in contact
1202 with the placodal *Tg(neurog1:GFP)+ or Tg(omp:meYFP)+* clusters. **M-P.** % of OPs with zero,
1203 one or two and more Activated Caspase 3 positive cells or debris in the OP or very close to the
1204 OP at 16, 21, 28 and 36 hpf in control embryos and *sly* mutants. Chi2 test. **Q, R.** Total number of
1205 YFP+ cells in control and mutant *Tg(omp:meYFP)+* OPs at 28 hpf (Q) and 36 hpf (R) (n = 3
1206 control placodes; n = 3 mutant placodes for each stage). Unpaired, two-tailed t test.

1207

1208 **Figure S3. Additional results on the OP morphogenesis defects observed in *sly* mutants**.
1209 **A-L.** Analysis of OP dimensions at 24, 28 and 32 hpf. **A, A', E, E' and I, I'.** Images (frontal
1210 views, 1 z-section) of representative OPs from *Tg(omp:meYFP); sly* $^{-/-}$ mutants (right) and control
1211 *Tg(omp:meYFP)* siblings (left) at 24 (A, A'), 28 (E, E') and 32 hpf (I, I'). **B-D.** Graphs showing the
1212 AP, ML, and DV dimensions of the *Tg(omp:meYFP)*$^{+}$ OP clusters in *sly* mutants and control
1213 siblings at 24 hpf (n = 10 controls and n = 10 mutants from 3 independent experiments). Ectopic
1214 fluorescent cells (cells that are physically separated from the main cluster) were not taken into
1215 account for the measurement of OP dimensions**.** Unpaired, two-tailed t test. **F-H**. Similar
1216 quantifications at 28 hpf (n = 13 controls and n = 10 mutants from 2 independent experiments).
1217 Unpaired, two-tailed t tests. **J-L**. Similar quantifications at 32 hpf (n = 17 controls and n = 13
1218 mutants from 2 independent experiments). Unpaired, two-tailed t tests. Quantifications
1219 performed at 36 hpf are shown in Fig. 4C-E. **M, N.** Examples of 2D tracks plotted in a lateral
1220 view (AP along X and DV along Y) of *Tg(omp:meYFP)*$^{+}$ OP cells (red) and adjacent brain cells
1221 (green) in a control (M) and a *sly* mutant embryo (N). The time is color-coded: light colors at the
1222 beginning of the trajectory (22 hpf) towards dark colors for the end of the track (1080 min later).
1223

1224 **Figure S4. Additional results for the analysis of brain shape and proliferation/apoptosis in**
1225 ***sly* mutants and control siblings. A, A'.** Immunostaining for HuC (cyan) at 28 hpf performed
1226 on *Tg(cldnb:Gal4; UAS:RFP)* (magenta) control and *sly* mutant embryos (frontal view). Similar
1227 immunostainings performed at 36 hpf are shown in Fig. 5A, A'. **B, B'**. Images of
1228 *Tg(elementC:gfp); Tg(cldnb:Gal4; UAS:RFP)* control and mutant embryos at 28 hpf (frontal
1229 view), similar images acquired at 36 hpf are shown in Fig. 5B, B'. GFP (green) is expressed by
1230 the forebrain, and a few OP cells. Arrows indicate where the thickness of the forebrain was
1231 measured (in 3 distinct positions along the DV axis). Measurements were also carried out at 3
1232 distinct AP levels (through the z-stack). **C, D.** Width of the forebrain in 28 hpf controls and *sly*
1233 mutants, at 3 different DV and 3 different AP levels (n = 17 controls and n = 17 mutants from 5
1234 independent experiments, unpaired, two-tailed t test). Quantifications for the 28 hpf stage are
1235 shown in Fig. 5C, D. **E-H.** Number of Phospho-histone H3 positive cells in the brain at 16, 21, 28
1236 and 36 hpf in control embryos and *sly* mutants. Unpaired, two-tailed t test. **I-L.** % of embryos
1237 with zero, one or two and more Activated Caspase 3 positive cells or debris in the brain at 16,
1238 21, 28 and 36 hpf in control embryos and *sly* mutants. Chi2 test.
1239

1240 **Figure S5. Additional results on olfactory axon development in *sly* mutants and control**
1241 **siblings. A, B.** Images extracted from confocal live imaging experiments performed during OP
1242 coalescence on *Tg(cldnb:Gal4; UAS:RFP)* embryos injected with the *neurog1:GFP* plasmid,
1243 allowing a sparse labelling of *neurog1:GFP*+ neurons/axons. The pictures illustrate instances of
1244 retrograde axon extension/cell body mediolateral movement occuring in a *sly* mutant and a
1245 control sibling. Arrows = proximal portions of the axons extending in the OP. Dotted line =
1246 brain/OP boundary (identified with the RFP signal which is not shown here). op = olfactory
1247 placode, b = brain. Scale bar: 20 µm. **C-F.** Images (frontal view, 1 z-section) of representative
1248 OPs from *Tg(omp:meYFP); sly* $^{-/-}$ mutant (E, F) and control *Tg(omp:meYFP)* siblings (C, D) at 24
1249 hpf. Arrows = instances of proximal portions of the axons in the OP. **G.** Table describing the %
1250 of control and *sly* mutant *Tg(omp:meYFP)* embryos with a proper axonal bundle (left column),
1251 with at least one ventral projection (middle column) and with at least one medial projection (right
1252 column) at 24, 28, 32 and 36 hpf. The numbers of embryos analysed at each stage are indicated
1253 in the table. The schematic view under the table illustrates the phenotypes assessed in each
1254 column. Note that in the mutants, as shown on the schematics, when a proper axon bundle is
1255 observed (left column), the exit point of the axons is more dorsal than in controls (see Fig. 4A,B
1256 and Fig. S3E,E' for instance).
1257
1258 **Figure S6. NCC defects in *sly* mutants. A, A'.** *In situ* hybridisation for the NCC marker *crestin*
1259 on 32 hpf controls and *sly* mutants. Arrowheads = *crestin*-positive NCC cluster at the OP/brain
1260 interface, which is absent in *sly* mutants. **B.** Table reporting our observations from live imaging
1261 of cranial NCC migration in *sly* mutants and control siblings (see Movie 9). Confocal live imaging
1262 was performed from 16 to 32 hpf on *sly* mutant and control *Tg(neurog1:GFP);Tg(UAS:RFP)*
1263 embryos injected with the *sox10(7.2):KalTA4* plasmid, allowing a mosaïc labelling of NCC.
1264
1265 **Figure S7. Olfactory system development in *foxd3* mutants. A, B**. *In situ* hybridisation for the
1266 NCC marker *crestin* on 32 hpf controls and *foxd3* mutants. Arrowheads = *crestin*-positive NCC
1267 cluster at the OP/brain interface, which is absent in *foxd3* mutants. **C, D**. Images (frontal view,
1268 maximum projection) of representative OPs of *Tg(omp:meYFP); foxd3* $^{-/-}$ mutants and control
1269 siblings. **C', D'**. Laminin immunostaining (1 z-section) on the same embryos. **E-H.** OP
1270 dimensions and length of the axon bundle at 28 hpf in *foxd3* mutants and control siblings (n = 31
1271 controls and n = 13 mutants from 2 independent experiments, unpaired, two-tailed t test). **I-L.**
1272 OP dimensions and length of the axon bundle in *foxd3* mutants and control siblings at 36 hpf (n
1273 = 21 controls and n = 4 mutants from 2 independent experiments, unpaired, two-tailed t test).

1274 **Legends of the movies**

1275 **Movie 1. BM assembly around the brain and the OP during OP coalescence**, related to Fig.
1276 1**.** Same embryo as the z-section shown in Fig. 1J. Confocal live imaging performed on a
1277 *TgBAC(lamC1:lamC1-sfGFP);Tg(cldnb:Gal4;UAS:RFP)* embryo in which Laminin *γ*1-sfGFP is
1278 expressed under the control of its own promoter (green), and OP and peridermal skin cells are
1279 labelled in with cytoplasmic RFP (magenta). Pink arrowheads indicate the BM surrounding the
1280 brain, which is already assembled and continuous when the movie starts (at 17 hpf), while the
1281 BM surrounding the OP (shown with yellow arrowheads) starts to assemble later, during OP
1282 coalescence. Grey dots indicate mesenchymal cells exhibiting Laminin *γ*1-sfGFP cytoplasmic
1283 expression and migrating around the OP. Yellow dots indicate RFP-positive OP cells also
1284 showing Laminin *γ*1-sfGFP cytoplasmic expression. Only the left side of the embryo is shown.
1285 One z-section, dorsal view, anterior to the top and lateral to the left, delta t = 10 min. Scale bar:
1286 25 µm.

1287 **Movie 2. Formation of the exit and entry points in the BMs surrounding the OP and the**
1288 **brain,** related to Fig. 1. Same embryo as the z-sections shown in Fig. 1E-I and in Movie 4.
1289 Confocal live-imaging performed on a *TgBAC(lamC1:lamC1-sfGFP);Tg(cldnb:Gal4;UAS:RFP)*
1290 embryo in which Laminin *γ*1-sfGFP is expressed under the control of its own promoter (green),
1291 and OP and peridermal skin cells are labelled in with cytoplasmic RFP (magenta). The yellow
1292 arrowhead shows the exit point, which appears as a small interruption (or several small
1293 interruptions, see also Movie 4) in the BM of the OP resulting from its incomplete assembly in
1294 this specific area. The blue arrowhead indicates the opening of the entry point (which can also
1295 be formed by several gaps in somes instances, ses also Movie 4) in the already assembled BM
1296 of the brain, which is concomitant with the arrival of the RFP-positive axons. Pink dots indicate
1297 brain cells expressing Laminin *γ*1-sfGFP cytoplasmic expression. Only the left side of the
1298 embryo is shown. One z-section, frontal view, dorsal to the top and lateral to the left, delta t = 10
1299 min. Scale bar: 25 µm.

1300 **Movie 3. Formation of the exit and entry points in the BMs surrounding the OP and the**
1301 **brain visualised with a mosaic labelling of OP axons,** related to Fig. 1. Confocal live-imaging
1302 performed on a *TgBAC(lamC1:lamC1-sfGFP);Tg(cldnb:Gal4;UAS:lyn-TagRFP)* embryo in which
1303 Laminin *γ*1-sfGFP is expressed under the control of its own promoter (green), and OP and
1304 peridermal skin cells are mosaically labelled in with membrane TagRFP (magenta). The yellow
1305 arrowhead shows the exit point on the last timepoint of the first movie, which appears as a small

1306 interruption (or several small interruptions) in the BM of the OP resulting from its incomplete
1307 assembly in this specific area. A lyn-TagRFP-positive individual axon can be seen exiting the
1308 OP through the exit point. The blue arrowhead indicates the opening of the entry point (which
1309 can also be formed by several gaps in some instances) in the already assembled BM of the
1310 brain, which is concomitant with the arrival of a few lyn-TagRFP-labelled axons. Only the left
1311 side of the embryo is shown. Average projection of 2 consecutive z-sections (z-step of 1 µm),
1312 frontal view, dorsal to the top and lateral to the left, delta t = 10 min. Scale bar: 25 µm.

1313 **Movie 4**. **3D z-stacks showing the exit and entry points**, related to Fig. 1. Same embryo as
1314 the z-sections shown in Fig. 1E-I and Movie 2. Confocal z-stacks performed on a live
1315 *TgBAC(lamC1:lamC1-sfGFP);Tg(cldnb:Gal4;UAS:RFP)* embryo in which Laminin γ1-sfGFP is
1316 expressed under the control of its own promoter (green), and OP and peridermal skin cells are
1317 labelled in with cytoplasmic RFP (magenta). The two z-stacks correspond to the last time points
1318 of the two time-lapses showing exit and entry point formation in single z-sections in Movie 2. The
1319 yellow arrowheads point to several interruptions in the BM of the OP (exit point). The blue
1320 arrowheads indicate the opening of several gaps in the BM of the brain (entry point). Only the
1321 left side of the embryo is shown. Frontal view, dorsal to the top, the first z-sections are the most
1322 anterior and the z-stacks progressively goes posterior, z-step of 1 µm. Scale bar: 25 µm.

1323 **Movie 5. OP coalescence in a control embryo and a *sly* mutant,** related to Fig. 3. Same
1324 embryos as the images and analyses shown in Fig. 3F-I. Confocal live imaging showing OP
1325 coalescence movements in *sly* mutant and control *Tg(neurog1:GFP)* embryos, in which OP and
1326 brain neurons are labelled with cytoplasmic GFP. On the last time point, the dotted lines outline
1327 the OPs. Note that on the *sly* mutant movie, a marked drift movement occurs at t = 170 min,
1328 which has been taken into account and substracted from the data in our cell tracking analysis.
1329 These embryos were injected with H2B-RFP mRNA to label nuclei and allow individual cell
1330 tracking (not shown). Average projection, dorsal view, anterior to the top, delta t = 10 min. Scale
1331 bar: 50 µm.

1332 **Movie 6. Behaviour of the OP neurons during the brain flexure movement in a control**
1333 **embryo and a *sly* mutant**, related to Fig. 4. Same embryos as the images and analyses shown
1334 in Figure 4I-L. Confocal live imaging showing OP cell movements and axon behaviours in *sly*
1335 mutant and control *Tg(omp:meYFP)* embryos, in which *ompb*-expressing OP neurons and their
1336 axons are labelled with membrane YFP. Note the global ventral movement occuring during the
1337 time-lapse, which corresponds to the movements of the OPs accompanying the brain flexure.

1338 These embryos were injected with H2B-RFP mRNA to label nuclei and allow individual cell
1339 tracking (not shown). Maximum projection, frontal view, dorsal to the top, delta t = 10 min. Scale
1340 bar: 50 µm.

1341 **Movie 7. 3D stacks showing the organisation of brain and OP neurons in control embryos**
1342 **and *sly* mutants**, related to Fig. 5 and Fig. S4. *sly* mutant and control *Tg(cldnb:Gal4;UAS:RFP)*
1343 embryos, in which OP and peridermal skin cells are labelled in with cytoplasmic RFP (magenta),
1344 were immunostained for HuC (cyan) at 28 hpf and 36 hpf to visualise the neurons in the OP and
1345 the brain. Note that in control embryos, the frontier between the OP and the brain appears as a
1346 straight line whereas in mutant embryos, the boundary between the two tissues is curved and
1347 not well defined, and the OPs appear to be partially embedded into the brain tissue. Frontal
1348 views, dorsal to the top, the first z-sections are the most anterior and the z-stack progressively
1349 goes posterior, z-step of 1 µm. Scale bar: 50 µm.

1350 **Movie 8. 3D stacks showing the axonal defects and ectopic OP cells observed in *sly***
1351 **mutants,** related to Fig. 4 and Fig. S5. The embryos are at 28 hpf and carry
1352 the *Tg(omp:meYFP)* transgene to visualise the membrane of *ompb*-expressing OP neurons and
1353 their axons (green). In control embryos, the bundle of axons exit the OP in a ventral position and
1354 migrate dorsally towards the presumptive OB. In mutant embryos, only a few axons manage to
1355 exit the OP in a dorsal position and reach the presumptive OB (white arrow). Most of them
1356 appear to be stalled at the OP/brain boundary (grey arrow). The mutant embryo also exhibits
1357 ectopic OP cells that are detached from the main OP cluster (magenta dots). White dots indicate
1358 the centre of the rosette of OP neurons that assemble in the dorso-lateral region of the OP. Only
1359 the left side of the embryo is shown. Frontal views, dorsal to the top, lateral to the left, the first z-
1360 sections are the most anterior and the z-stack progressively goes posterior, z-step of 1 µm.
1361 Scale bar: 25 µm.

1362 **Movie 9. NCC migration in *sly* mutants and control siblings**, related to Fig. S6**.** Confocal live
1363 imaging from 16 to 32 hpf showing OP and NCC cell movements in *sly* mutant and control
1364 *Tg(neurog1:GFP);Tg(UAS:RFP)* embryos injected with the *sox10(7.2):KalTA4* plasmid. The
1365 DNA injection in this transgenic background allows the mosaic RFP labelling of NCC and their
1366 derivatives. Note that in the mutant, a few neuroepithelial brain cells also express RFP. The blue
1367 arrowheads point to instances of NCC migrating between the eye and OP tissues, the yellow
1368 arrowheads indicate some NCC populating the OP/forebrain interface. In the *sly* mutant embryo,

1369 the NCC migrating at the OP/forebrain boundary appear to be expelled from the interface, and
1370 one of them eventually dies. Only the left side of the embryo is shown. Average projection,
1371 dorsal view, lateral to the left, delta t = 10 min. Scale bar: 20 μm.

1372

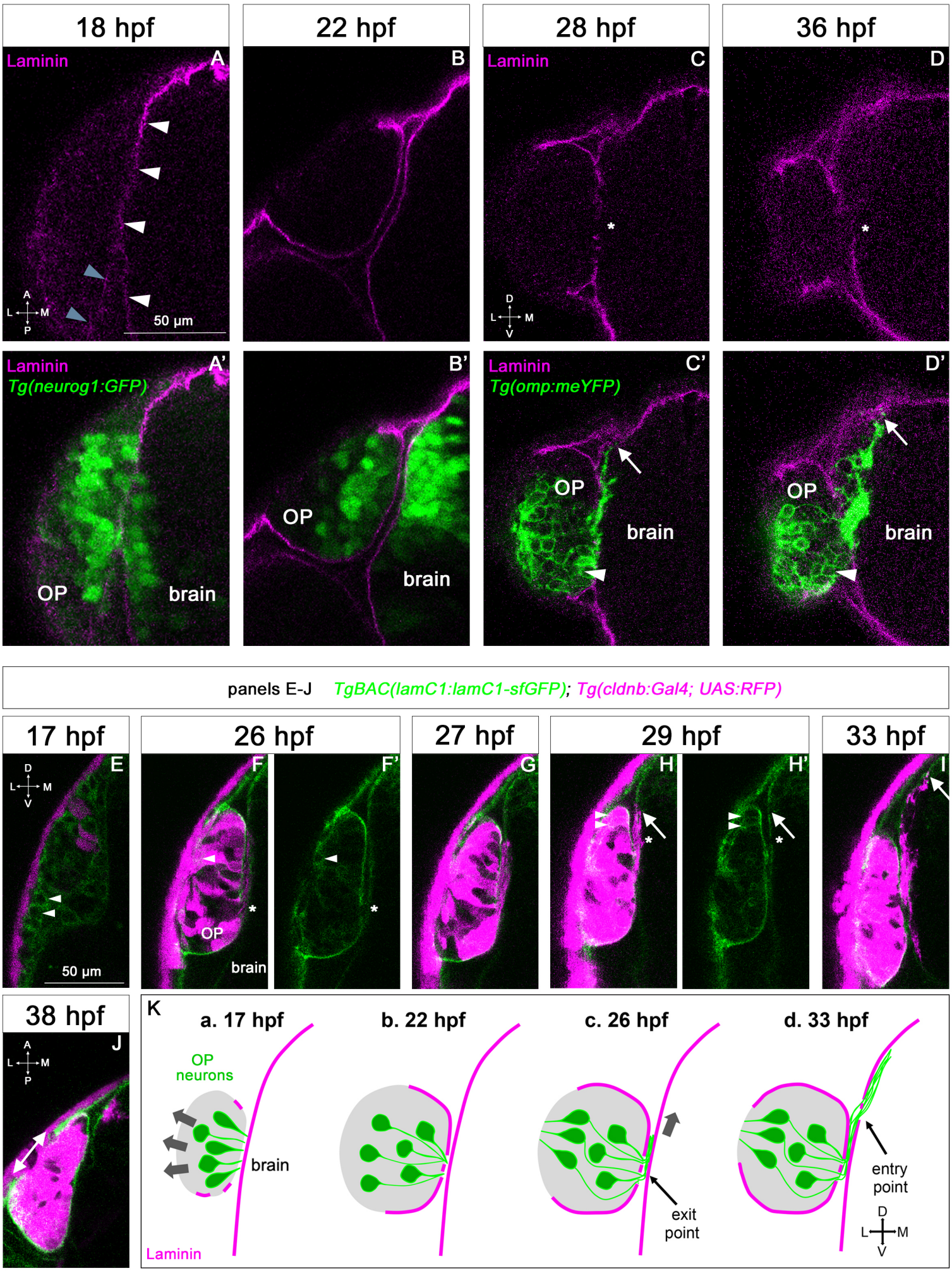
18 hpf
22 hpf
28 hpf
36 hpf
Laminin
A
B
C
D
50 µm
A'
B'
C'
D'
Tg(neurog1:GFP)
Tg(omp:meYFP)
OP
brain
panels E-J
TgBAC(lamC1:lamC1-sfGFP); Tg(cldnb:Gal4; UAS:RFP)
17 hpf
26 hpf
27 hpf
29 hpf
33 hpf
E
F
F'
G
H
H'
I
38 hpf
J
K
a. 17 hpf
b. 22 hpf
c. 26 hpf
d. 33 hpf
OP neurons
entry point
exit point

Figure 1

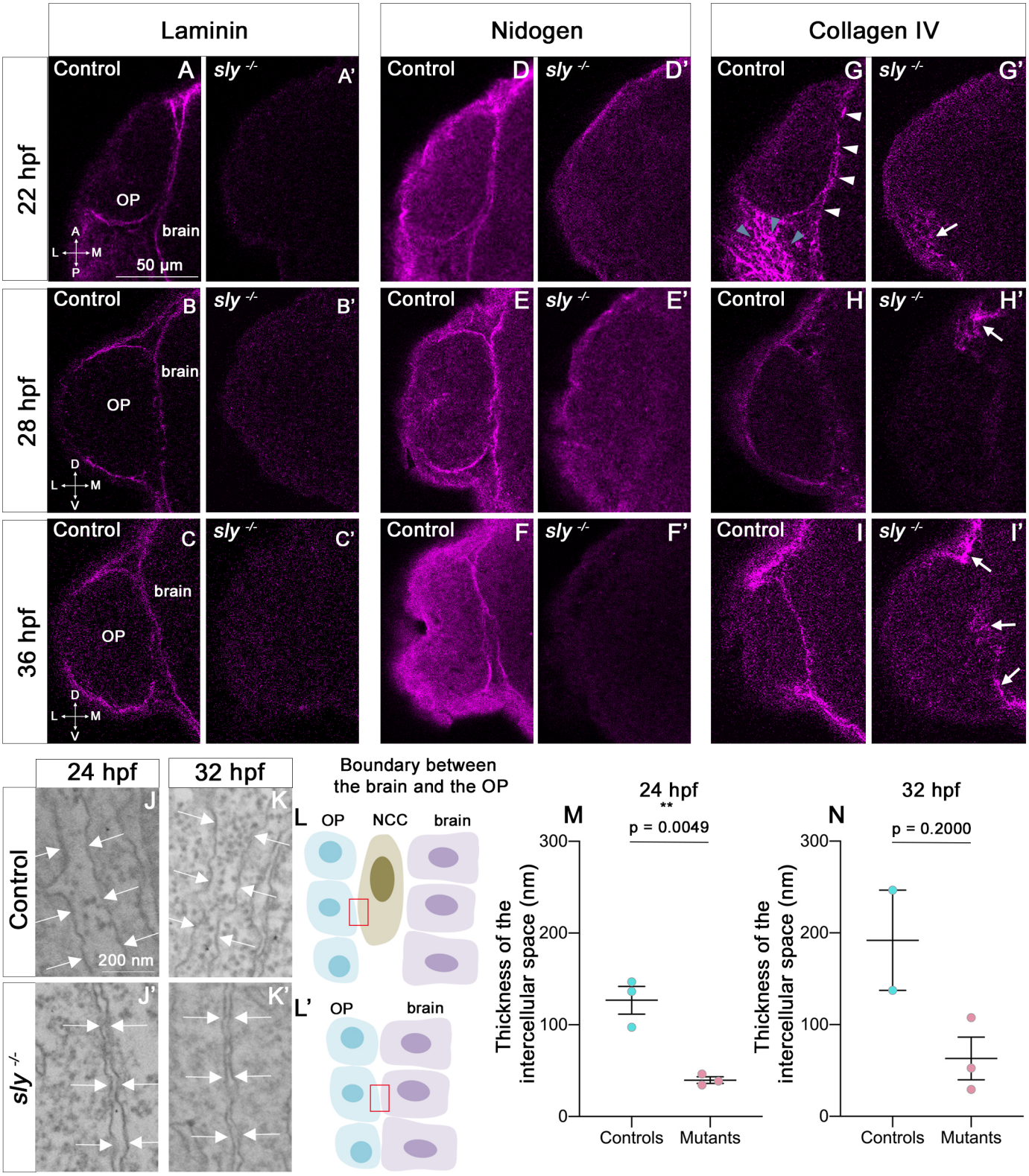
Laminin
Nidogen
Collagen IV
22 hpf
28 hpf
36 hpf
Control
sly -/-
A
A'
B
B'
C
C'
D
D'
E
E'
F
F'
G
G'
H
H'
I
I'
OP
brain
50 µm
A
P
L
M
D
V
24 hpf
32 hpf
J
K
J'
K'
200 nm
Boundary between
the brain and the OP
L
L'
OP
NCC
brain
M
N
24 hpf
32 hpf
**
p = 0.0049
p = 0.2000
Thickness of the
intercellular space (nm)
300
200
100
0
Controls
Mutants

Figure 2

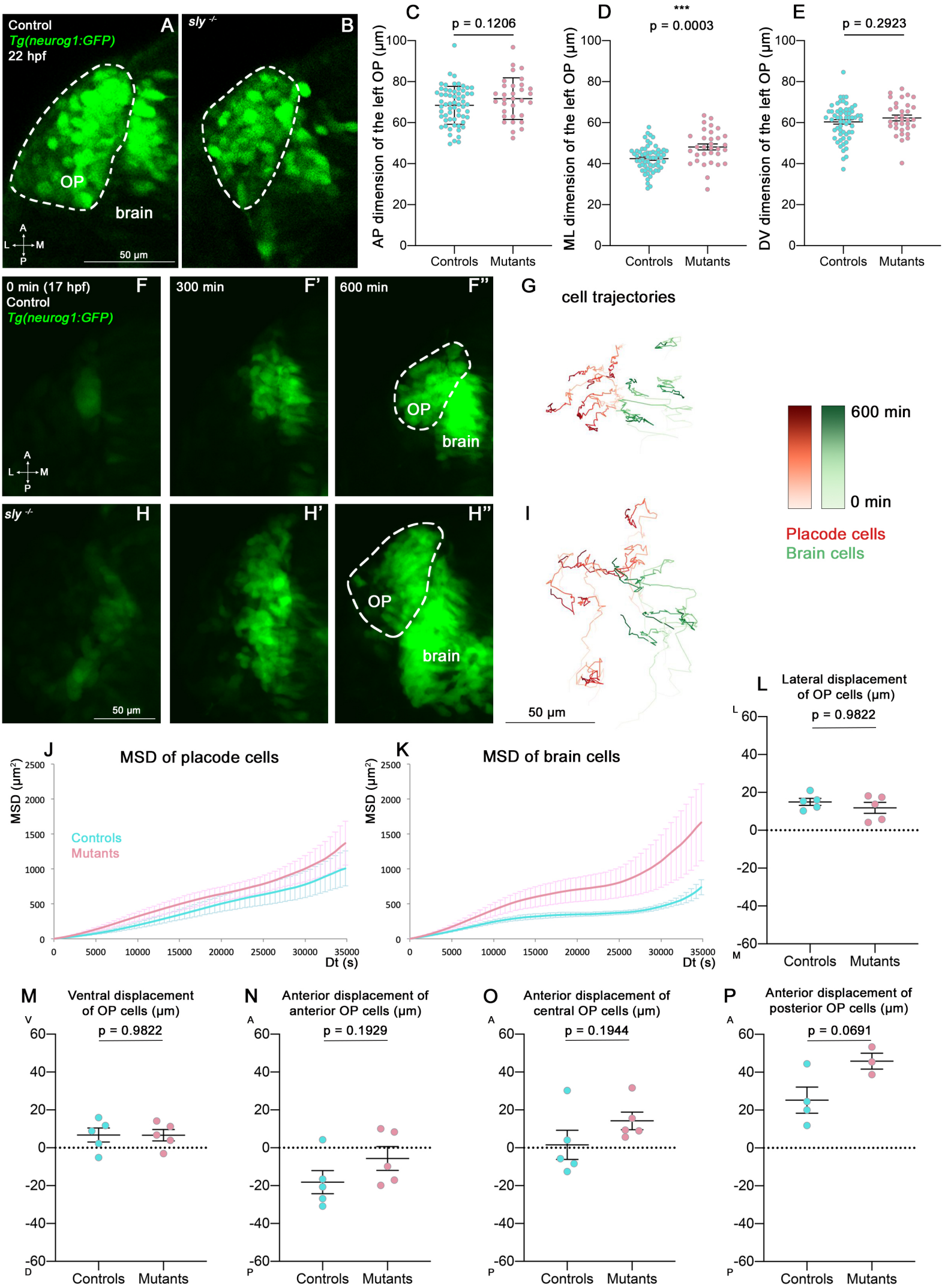
Control
Tg(neurog1:GFP)
22 hpf
A
OP
brain
A
L
M
P
50 µm
sly -/-
B
C
p = 0.1206
AP dimension of the left OP (µm)
Controls
Mutants
D
***
p = 0.0003
ML dimension of the left OP (µm)
E
p = 0.2923
DV dimension of the left OP (µm)
0 min (17 hpf)
Control
Tg(neurog1:GFP)
F
300 min
F'
600 min
F''
G
cell trajectories
600 min
0 min
Placode cells
Brain cells
sly -/-
H
H'
H''
I
50 µm
J
MSD of placode cells
MSD (µm²)
Controls
Mutants
Dt (s)
K
MSD of brain cells
L
Lateral displacement of OP cells (µm)
p = 0.9822
M
Ventral displacement of OP cells (µm)
p = 0.9822
N
Anterior displacement of anterior OP cells (µm)
p = 0.1929
O
Anterior displacement of central OP cells (µm)
p = 0.1944
P
Anterior displacement of posterior OP cells (µm)
p = 0.0691

Figure 3

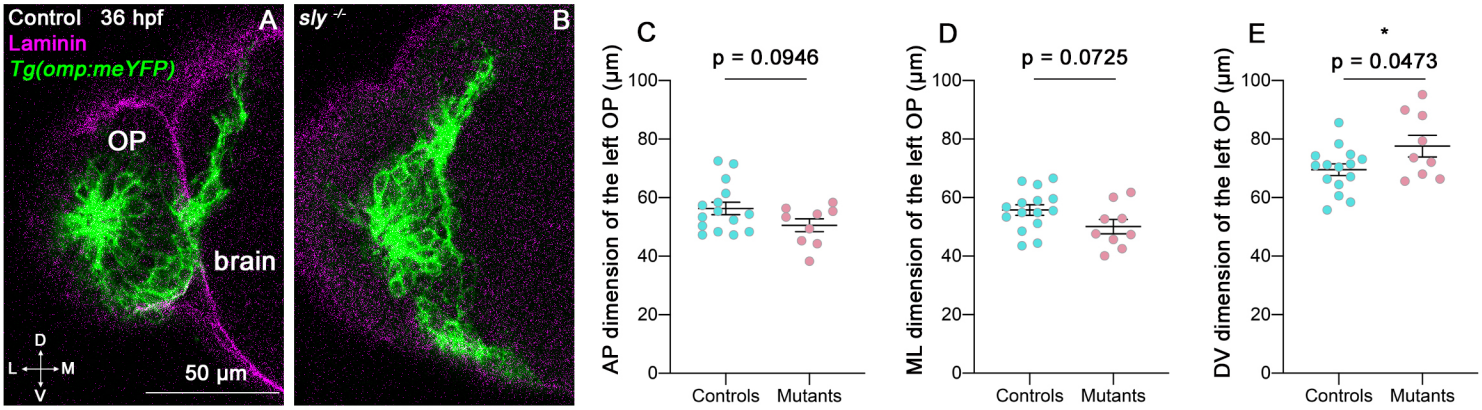

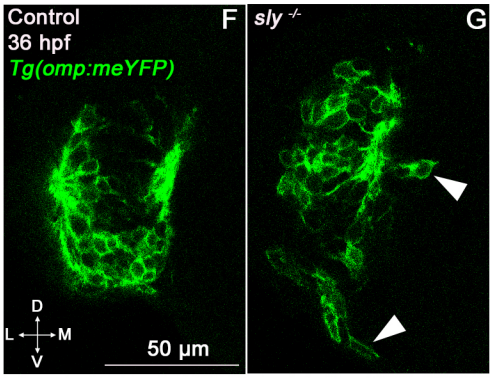

H

% of embryos with		Dorsal ectopic cells	Ventral ectopic cells	Lateral ectopic cells	Medial ectopic cells
24 hpf	Controls (n = 11)	0 %	55%	0 %	9%
	Mutants (n = 10)	40 %	100 %	0 %	50 %
28 hpf	Controls (n = 14)	14 %	21 %	0 %	14 %
	Mutants (n = 11)	64 %	100 %	18 %	73 %
32 hpf	Controls (n = 17)	6 %	12 %	6 %	6 %
	Mutants (n = 13)	54 %	100 %	23 %	77 %
36 hpf	Controls (n = 16)	6 %	13 %	0 %	0 %
	Mutants (n = 10)	60 %	100 %	40 %	30 %

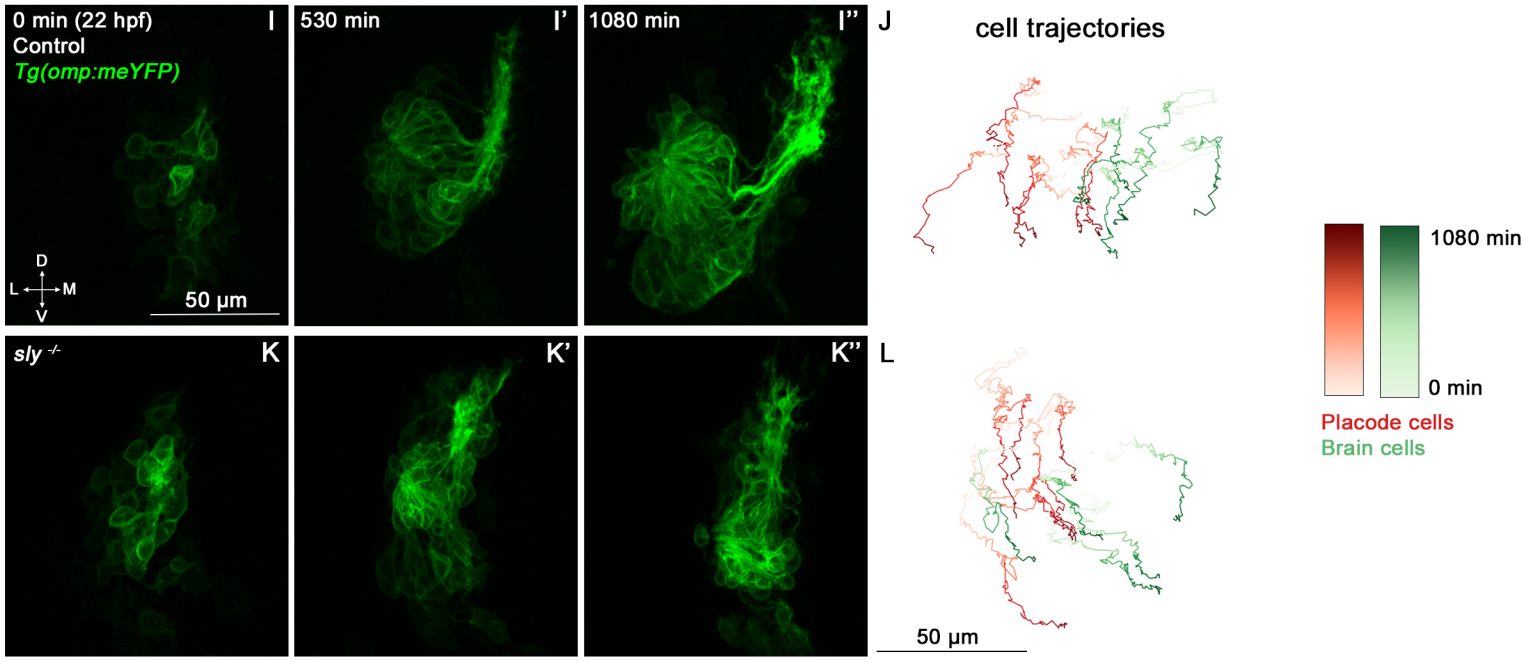

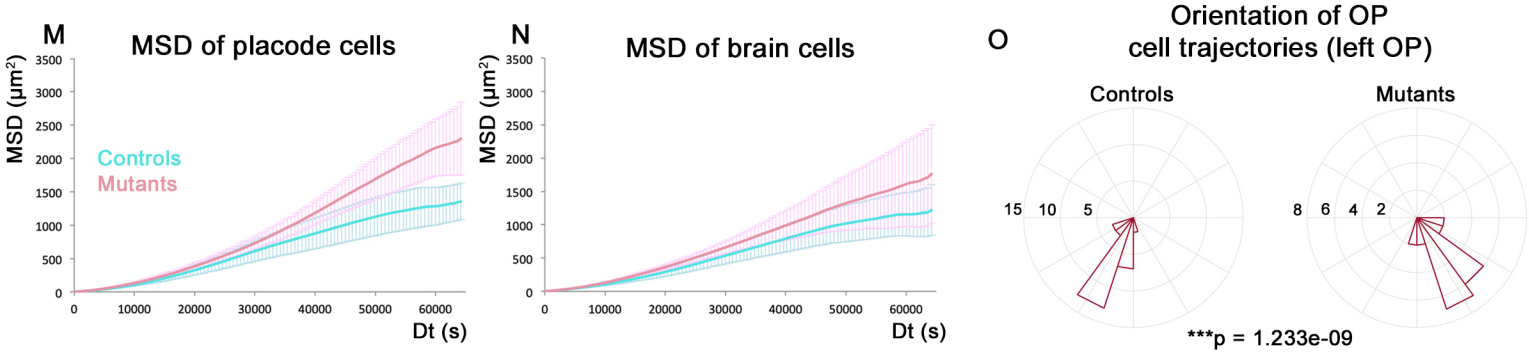

Figure 4

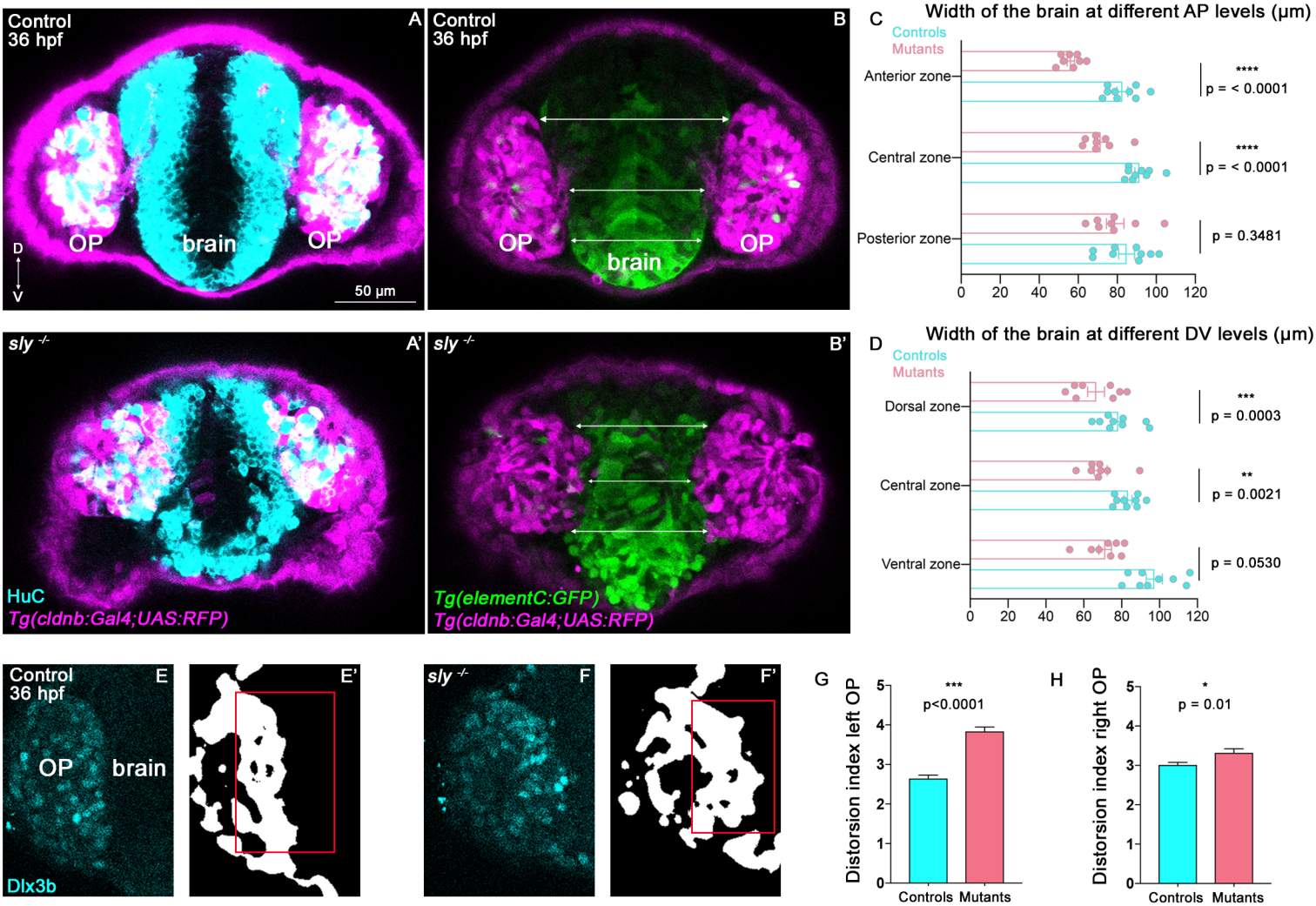
Control
36 hpf
A
OP
brain
OP
D
V
50 µm
Control
36 hpf
B
OP
brain
OP
C
Width of the brain at different AP levels (µm)
Controls
Mutants
Anterior zone
Central zone
Posterior zone
****
p = < 0.0001
****
p = < 0.0001
p = 0.3481
0
20
40
60
80
100
120
sly -/-
A'
HuC
Tg(cldnb:Gal4;UAS:RFP)
sly -/-
B'
Tg(elementC:GFP)
Tg(cldnb:Gal4;UAS:RFP)
D
Width of the brain at different DV levels (µm)
Controls
Mutants
Dorsal zone
Central zone
Ventral zone
***
p = 0.0003
**
p = 0.0021
p = 0.0530
0
20
40
60
80
100
120
Control
36 hpf
E
OP
brain
Dlx3b
E'
sly -/-
F
F'
G
Distorsion index left OP
***
p<0.0001
Controls
Mutants
H
Distorsion index right OP
*
p = 0.01
Controls
Mutants

Figure 5

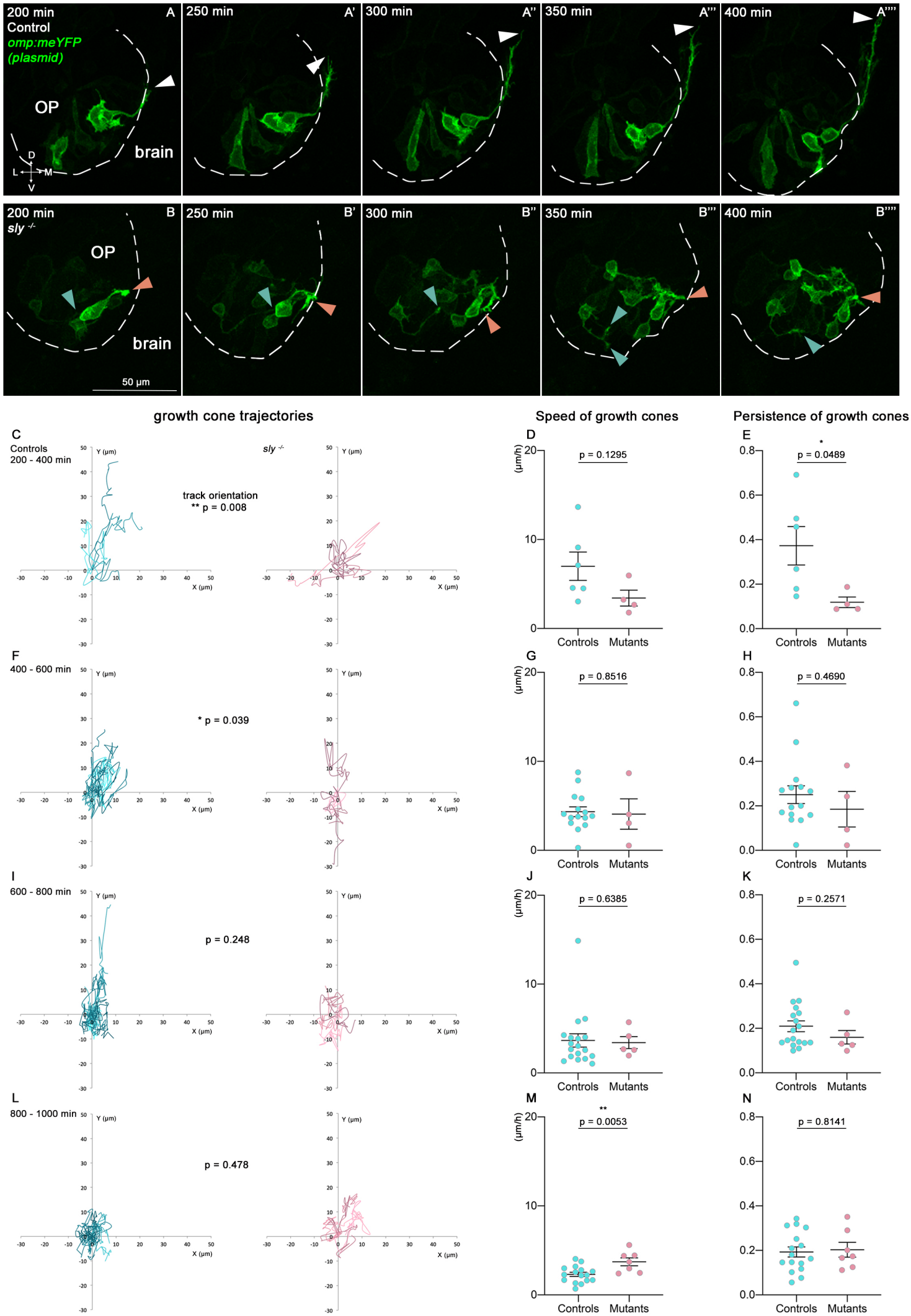
200 min
Control
omp:meYFP
(plasmid)
A
250 min
A'
300 min
A''
350 min
A'''
400 min
A''''
OP
brain
D
L
M
V
200 min
sly -/-
B
250 min
B'
300 min
B''
350 min
B'''
400 min
B''''
OP
brain
50 µm
growth cone trajectories
Speed of growth cones
Persistence of growth cones
C
Controls
200 - 400 min
sly -/-
track orientation
** p = 0.008
D
p = 0.1295
E
*
p = 0.0489
F
400 - 600 min
* p = 0.039
G
p = 0.8516
H
p = 0.4690
I
600 - 800 min
p = 0.248
J
p = 0.6385
K
p = 0.2571
L
800 - 1000 min
p = 0.478
M
**
p = 0.0053
N
p = 0.8141
Y (µm)
X (µm)
(µm/h)
Controls
Mutants

Figure 6